J. Fluid Mech. (2012), *vol.* 699, *pp.* 385–413. © Cambridge University Press 2012
doi:10.1017/jfm.2012.115

Dynamic *k*-equation model for large-eddy simulation of compressible flows

Xiaochuan Chai and Krishnan Mahesh†

Aerospace Engineering and Mechanics, University of Minnesota, Minneapolis, MN 55108, USA

(Received 5 May 2011; revised 3 January 2012; accepted 26 February 2012;
first published online 16 April 2012)

This paper presents a dynamic one-equation eddy viscosity model for large-eddy simulation (LES) of compressible flows. The transport equation for subgrid-scale (SGS) kinetic energy is introduced to predict SGS kinetic energy. The exact SGS kinetic energy transport equation for compressible flows is derived formally. Each of the unclosed terms in the SGS kinetic energy equation is modelled separately and dynamically closed, instead of being grouped into production and dissipation terms, as in the Reynolds averaged Navier–Stokes equations. All of the SGS terms in the filtered total energy equation are found to reappear in the SGS kinetic energy equation. Therefore, these terms can be included in the total energy equation without adding extra computational cost. *A priori* tests using direct numerical simulation (DNS) of decaying isotropic turbulence show that, for a Smagorinsky-type eddy viscosity model, the correlation between the SGS stress and the model is comparable to that from the original model. Also, the suggested model for the pressure dilatation term in the SGS kinetic energy equation is found to have a high correlation with its actual value. In *a posteriori* tests, the proposed dynamic *k*-equation model is applied to decaying isotropic turbulence and normal shock–isotropic turbulence interaction, and yields good agreement with available experimental and DNS data. Compared with the results of the dynamic Smagorinsky model (DSM), the *k*-equation model predicts better energy spectra at high wavenumbers, similar kinetic energy decay and fluctuations of thermodynamic quantities for decaying isotropic turbulence. For shock–turbulence interaction, the *k*-equation model and the DSM predict similar evolutions of turbulent intensities across shocks, owing to the dominant effect of linear interaction. The proposed *k*-equation model is more robust in that local averaging over neighbouring control volumes is sufficient to regularize the dynamic procedure. The behaviour of pressure dilatation and dilatational dissipation is discussed through the budgets of the SGS kinetic energy equation, and the importance of the dilatational dissipation term is addressed.

Key words: compressible turbulence, high-speed flow, shock waves

1. Introduction

Large-eddy simulation (LES) has gained great success in simulating practical flows where the Reynolds numbers are usually very high. By calculating the large-scale fluid motions directly from the filtered Navier–Stokes equations while modelling

† Email address for correspondence: mahesh@aem.umn.edu

https://doi.org/10.1017/jfm.2012.115 Published online by Cambridge University Press

the unresolved motions, LES alleviates the Reynolds number restrictions in direct numerical simulation (DNS), but preserves the ability to present the instantaneous flow characteristics and turbulent flow structures. The Smagorinsky model (Smagorinsky 1963; Lilly 1967) is an eddy viscosity model that contains a model coefficient C_s that must be determined *a priori*. However, C_s is problem-dependent, and in principle should be a function of time and space. To avoid the need to prescribe or tune the model coefficient, Germano *et al.* (1991) devised the dynamic Smagorinsky model (DSM), where the model coefficient is dynamically calculated during the simulation using the resolved scales. The dynamic procedure uses the assumption of scale invariance by applying the coefficient obtained from the resolved scales to the subgrid scale (SGS) range. This is referred to as the Germano identity and has become the basis of several dynamic models.

Many variants of the Smagorinsky model have been developed, such as SGS kinetic energy models (Lilly 1967; Deardorff 1973; Schumann 1975), spectral eddy viscosity models (Kraichnan 1976; Chollet & Lesieur 1981) and structure function models (Yakhot, Orszag & Yakhot 1989; Métais & Lesieur 1992; Smith & Woodruff 1998). The reader is referred to the review papers by Lesieur & Métais (1996) and Meneveau & Katz (2000) for past SGS model developments. Most of these models have either been developed for incompressible flows or are restricted to flows with simple geometries. Relatively few models have been developed for compressible flows. The compressible DSM model developed by Moin *et al.* (1991) is still the most popular model used in simulations of compressible flows. As opposed to incompressible flows, the SGS kinetic energy has to be modelled explicitly in compressible LES. The most commonly used model for SGS kinetic energy is Yoshizawa's model (Yoshizawa 1986), which is derived from the multiscale direct interaction approximation (Kraichnan 1964). Speziale *et al.* (1988) showed that Yoshizawa's model is only applicable to compressible flows with small density fluctuations, and correlates poorly with the DNS results of isotropic turbulence at low Mach numbers. They suggested that these limitations could be reduced based on Favre-filtered fields. In compressible DSM, Favre filtering is applied, and Yoshizawa's model is naturally generalized for SGS kinetic energy. Furthermore, Yoshizawa's model is based on the assumption of local equilibrium, i.e. the production of turbulent energy equals its dissipation, which is not the case most of the time. It has been shown that Yoshizawa's model tends to under-predict the magnitude of the SGS kinetic energy (Park & Mahesh 2007).

An alternative and original approach to derive SGS kinetic energy is by solving its transport equation. One-equation SGS models have been extensively used in incompressible large-eddy simulations (e.g. Lilly 1967; Deardorff 1973; Schumann 1975; Moeng 1984; Yoshizawa & Horiuti 1985; Shaw & Schumann 1992; Mason 1994; Ghosal *et al.* 1995; Menon & Kim 1996), and have shown success especially in the prediction of inhomogeneous turbulent flows. For example, Horiuti (1985) showed that the SGS kinetic energy equation model yielded improved performance compared to the Smagorinsky model in the simulation of rectangular channel flow. For compressible LES, works on one-equation SGS models are lacking. Therefore, here we develop a compressible version of the DSM with SGS kinetic energy equation, which will be referred to as dynamic k-equation model in the rest of the paper.

The localized dynamic k-equation model (LDKM), developed by Menon & Kim (1996), is an eddy viscosity model based on the SGS kinetic energy equation for incompressible flows. Recently, the LDKM has been extended for compressible flows and applied to the LES of a sonic jet injected into a supersonic cross-flow (Génin &

https://doi.org/10.1017/jfm.2012.115 Published online by Cambridge University Press

Menon 2010). Extra terms were added to the SGS kinetic energy equation to account for compressibility effects. Both the incompressible and compressible SGS kinetic energy equations used in the LDKM are simplified or modelled equations that appear to be adapted from the transport equations for turbulent kinetic energy (Speziale 1991). A different methodology is used for the dynamic procedure as well. In the current study, the exact compressible SGS kinetic energy equation is derived formally. Each of the unclosed terms is modelled separately instead of being grouped into production, dissipation, etc., so that the contribution of each term can be evaluated individually. For example, dilatational dissipation and solenoidal dissipation are modelled separately, unlike in Génin & Menon (2010), who note that modelling them together is subject to the assumption of low Mach number. Furthermore, all of the extra SGS terms (besides SGS stress and SGS heat flux) in the filtered total energy equation (Vreman, Geurts & Kuerten 1995; Garnier, Adams & Sagaut 2009) are found to reappear in the SGS kinetic energy equation, which allows us to take them into account without adding extra computational cost. The traditional Germano identity is applied to the dynamic closure for most SGS terms.

This paper derives the compressible SGS kinetic energy transport equation, and models the unclosed terms in energy equations and dynamically closes them. The proposed model is then incorporated into the parallel finite volume Navier–Stokes solver on unstructured grids developed by Park & Mahesh (2007) and applied to decaying isotropic turbulence and normal shock–isotropic turbulence interaction. The LES modelling background and the governing equations are introduced in § 2. Then § 3 discusses the derivation and modelling of the compressible SGS kinetic energy transport equation and the dynamic procedures as well. *A priori* tests are performed in § 4, followed by *a posteriori* tests (§ 5), where the LES results of isotropic turbulence and shock–turbulence interaction are presented. In § 6, the budgets of the SGS kinetic energy equation are evaluated, and the relevance of pressure dilatation and dilatational dissipation is discussed.

2. LES modelling background

LES decomposes flow variables into resolved (filtered) and SGS (residual) terms. For example, any flow variable can be decomposed as

$$\phi(x) = \bar{\phi}(x) + \phi'(x), \tag{2.1}$$

where

$$\bar{\phi}(x) = \int_{\Omega} G_{\Delta}(x, y)\phi(y)\,\mathrm{d}y \tag{2.2}$$

denotes the spatial filtering of $\phi(x)$, and $G_{\Delta}(x, y)$ is the kernel of the filter, which satisfies the normalization condition

$$\int_{\Omega} G_{\Delta}(x, y)\,\mathrm{d}y = 1. \tag{2.3}$$

In practice, especially for an unstructured flow solver, the filter is usually the grid filter, with the filter width Δ being a measure of local grid size. The filtered quantities are solved numerically from the filtered governing equations, which provides an approximation to the large-scale motions in the flow fields. Within the filtered governing equations, there are SGS stress terms representing the influence of SGS

https://doi.org/10.1017/jfm.2012.115 Published online by Cambridge University Press

motions on the resolved field. These SGS terms cannot be calculated directly and therefore are modelled in terms of resolved quantities.

2.1. *The filtered Navier–Stokes equations*

For compressible flow, the density-weighted (Favre) filtering is applied, i.e.

$$\tilde{\phi} = \frac{\overline{\rho\phi}}{\bar{\rho}}. \tag{2.4}$$

When Favre filtered, the spatially filtered compressible Navier–Stokes equations take the form

$$\frac{\partial \bar{\rho}}{\partial t} = -\frac{\partial(\bar{\rho}\widetilde{u_j})}{\partial x_j}, \tag{2.5}$$

$$\frac{\partial(\bar{\rho}\widetilde{u_i})}{\partial t} = -\frac{\partial}{\partial x_j}(\bar{\rho}\widetilde{u_i}\widetilde{u_j} + \bar{p}\delta_{ij} - \widetilde{\sigma_{ij}} + \tau_{ij}), \tag{2.6}$$

$$\frac{\partial}{\partial t}(\bar{\rho}\widetilde{E}) = -\frac{\partial}{\partial x_j}(\bar{\rho}\widetilde{E}\widetilde{u_j} + \bar{p}\widetilde{u_j} - \widetilde{\sigma_{ij}}\widetilde{u_i} - \overline{Q_j} + C_p q_j) + H, \tag{2.7}$$

$$\bar{p} = \bar{\rho}R\widetilde{T}, \tag{2.8}$$

where ρ, u_i, p and E are density, velocity, pressure and specific total energy, respectively. The viscous stress $\widetilde{\sigma_{ij}}$ and heat flux $\overline{Q_j}$ are given by

$$\widetilde{\sigma_{ij}} = 2\bar{\mu}\widetilde{S^*_{ij}}, \tag{2.9}$$

$$\overline{Q_j} = \bar{\kappa}\frac{\partial \widetilde{T}}{\partial x_j}, \tag{2.10}$$

where μ is the molecular viscosity, κ is the thermal conductivity, S^*_{ij} is the traceless strain-rate tensor, i.e.

$$\begin{aligned}\widetilde{S^*_{ij}} &= \widetilde{S_{ij}} - \tfrac{1}{3}\delta_{ij}\widetilde{S_{kk}} \\ &= \frac{1}{2}\left(\frac{\partial \widetilde{u_i}}{\partial x_j} + \frac{\partial \widetilde{u_j}}{\partial x_i}\right) - \frac{1}{3}\frac{\partial \widetilde{u_k}}{\partial x_k}\delta_{ij},\end{aligned} \tag{2.11}$$

and

$$\tau_{ij} = \bar{\rho}(\widetilde{u_i u_j} - \widetilde{u_i}\widetilde{u_j}), \tag{2.12}$$

$$q_j = \bar{\rho}(\widetilde{T u_j} - \widetilde{T}\widetilde{u_j}) \tag{2.13}$$

are the SGS stress and SGS heat flux, respectively. In (2.7), the expressions for E and H are

$$\bar{\rho}\widetilde{E} = C_v\bar{\rho}\widetilde{T} + \tfrac{1}{2}\bar{\rho}\widetilde{u_i}\widetilde{u_i} + \bar{\rho}k \tag{2.14}$$

and

$$\begin{aligned}H = &-\frac{\partial}{\partial x_j}\left[\frac{1}{2}(\bar{\rho}\widetilde{u_i u_i u_j} - \bar{\rho}\widetilde{u_i}\widetilde{u_i}\widetilde{u_j})\right] - \frac{\partial}{\partial x_j}\left[\frac{5}{3}\left(\bar{\mu}u_j\widetilde{\frac{\partial u_k}{\partial x_k}} - \bar{\mu}\widetilde{u_j}\frac{\partial \widetilde{u_k}}{\partial \widetilde{x_k}}\right)\right] \\ &+ \frac{\partial}{\partial x_j}\left[\bar{\mu}\frac{\partial k}{\partial x_j}\right] + \frac{\partial}{\partial x_j}\left[\bar{\mu}\frac{\partial}{\partial x_i}\left(\frac{\tau_{ij}}{\bar{\rho}}\right)\right],\end{aligned} \tag{2.15}$$

https://doi.org/10.1017/jfm.2012.115 Published online by Cambridge University Press

where k in (2.14) and (2.15) is the SGS kinetic energy defined by

$$\bar{\rho}k = \tfrac{1}{2}\tau_{kk} = \tfrac{1}{2}\bar{\rho}(\widetilde{u_k u_k} - \tilde{u}_k\tilde{u}_k). \tag{2.16}$$

Two assumptions have been made to derive the above equations. First, the filtering operations and derivatives are assumed to be commutative. Second, the kinematic viscosity ν, specific heats C_p and C_v, and Prandtl number Pr are assumed to be spatially uniform over the filter width, so that

$$\overline{\sigma_{ij}} = \overline{2\rho\nu S^*_{ij}} = 2\bar{\rho}\nu\widetilde{S}^*_{ij} = 2\bar{\mu}\widetilde{S}^*_{ij} = \widetilde{\sigma}_{ij} \tag{2.17}$$

and

$$\overline{Q_j} = \overline{\frac{\mu C_p}{Pr}\frac{\partial T}{\partial x_j}} = \frac{\bar{\mu}C_p}{Pr}\frac{\partial\widetilde{T}}{\partial x_j} = \bar{\kappa}\frac{\partial\widetilde{T}}{\partial x_j}. \tag{2.18}$$

The SGS stress, SGS heat flux and the first two terms in (2.15) cannot be computed directly from the resolved quantities. Models for these terms are discussed below.

2.2. *Dynamic Smagorinsky model (DSM)*

In the compressible DSM, the H term defined by (2.15) is assumed to be small and is neglected. The SGS stress and SGS heat flux terms are modelled by

$$\tau_{ij} - \frac{\delta_{ij}}{3}\tau_{kk} = -2C_s\bar{\rho}\Delta^2|\widetilde{S}|\widetilde{S}^*_{ij}, \tag{2.19}$$

$$q_j = -\bar{\rho}\frac{C_s\Delta^2|\widetilde{S}|}{Pr_T}\frac{\partial\tilde{T}}{\partial x_j}, \tag{2.20}$$

and Yoshizawa's formula is used to model $\tau_{kk} = 2\bar{\rho}k$, i.e.

$$\tau_{kk} = 2C_I\bar{\rho}\Delta^2\,|\widetilde{S}|^2, \tag{2.21}$$

where $|S| = \sqrt{2S_{ij}S_{ij}}$. The model coefficients C_s, C_I and Pr_T are determined dynamically by the Germano identity, which assumes similarity of SGS quantities between the grid filter level and test filter level; for any term $a = \overline{\alpha\beta} - \bar{\alpha}\bar{\beta}$, we assume that, on the test filter level, $A = \widehat{\overline{\alpha\beta}} - \hat{\bar{\alpha}}\hat{\bar{\beta}}$ holds. Here, $\hat{\cdot}$ denotes test filtering. The Germano identity is then defined by $L = A - \hat{a} = \widehat{\bar{\alpha}\bar{\beta}} - \hat{\bar{\alpha}}\hat{\bar{\beta}}$. Assume that the model for a is $a = Cm$, where m is a function of the resolved (grid filter level) quantities; then at the test filter level, $A = CM$, where M takes similar form to m but is a function of the test-filtered quantities. Substituting the models for A and a, the Germano identity becomes

$$L = \widehat{\bar{\alpha}\bar{\beta}} - \hat{\bar{\alpha}}\hat{\bar{\beta}} = C(M - \hat{m}). \tag{2.22}$$

Both sides of (2.22) may be calculated from the resolved variables, and the model coefficient C can be solved dynamically as

$$C = \frac{\widehat{\bar{\alpha}\bar{\beta}} - \hat{\bar{\alpha}}\hat{\bar{\beta}}}{(M - \hat{m})}. \tag{2.23}$$

The coefficient C varies with time and space. Finally, to avoid computational instability, C is regularized using a combination of least-square method (Lilly 1991)

https://doi.org/10.1017/jfm.2012.115 Published online by Cambridge University Press

and volume averaging, e.g. the formula for the model coefficient of SGS stress C_s is

$$C_s\Delta^2 = \frac{1}{2}\frac{\langle L_{ij}^* M_{ij}^* \rangle}{\langle M_{ij}^* M_{ij}^* \rangle}, \tag{2.24}$$

where

$$L_{ij} = \left(\widehat{\frac{\widehat{\overline{\rho u_i}}\;\widehat{\overline{\rho u_j}}}{\bar{\rho}}} \right) - \frac{\widehat{\overline{\rho u_i}}\;\widehat{\overline{\rho u_j}}}{\hat{\bar{\rho}}}, \tag{2.25}$$

$$L_{ij}^* = L_{ij} - \tfrac{1}{3}\delta_{ij} L_{kk}, \tag{2.26}$$

$$M_{ij}^* = \bar{\rho}\widehat{|\tilde{S}|\tilde{S}_{ij}^*} - \hat{\bar{\rho}}\left(\frac{\widehat{\Delta}}{\Delta}\right)^2 \widehat{|\tilde{S}|}\,\widehat{\tilde{S}_{ij}^*}. \tag{2.27}$$

Here, $\langle \cdot \rangle$ denotes the spatial average over homogeneous directions. Expressions for Pr_t in the SGS heat flux q_j and other details about the compressible DSM may be found in Moin *et al.* (1991).

3. Dynamic k-equation model

The key idea of the proposed dynamic k-equation model is to derive the SGS kinetic energy (or the isotropic part of the SGS stress, τ_{kk} in (2.19)) by solving its transport equation, instead of using Yoshizawa's model equation (2.21). It has been shown that Yoshizawa's model for the SGS stress correlates very poorly with the DNS results of compressible isotropic turbulence (Speziale *et al.* 1988), and under-predicts the magnitude of the SGS kinetic energy (Park & Mahesh 2007). On the other hand, the works of Deardorff (1973), Schumann (1975), Horiuti (1985), Ghosal *et al.* (1995) and Menon & Kim (1996) show that using the SGS kinetic energy equation yields better performance in large-eddy simulations of incompressible flows. Therefore, we extend this idea to compressible flows, and introduce the compressible SGS kinetic energy transport equation.

3.1. *SGS kinetic energy transport equation*

The SGS kinetic energy equation can be derived by subtracting the product of the Favre-filtered velocity and the filtered momentum equation from the filtered product of the velocity and momentum equation, i.e.

$$\overline{[u_i \times (\text{momentum equation})]} - \widetilde{u_i} \times \overline{(\text{momentum equation})}. \tag{3.1}$$

After reduction and rearrangement of the above equation, the SGS kinetic energy equation can be obtained as

$$\begin{aligned}\frac{\partial \bar{\rho} k}{\partial t} = &-\frac{\partial \bar{\rho} k \tilde{u}_j}{\partial x_j} - \tau_{ij}\widetilde{S}_{ij} - 2\bar{\mu}\left[\widetilde{S_{ij}^* D_{ij}^*} - \widetilde{S}_{ij}^* \widetilde{D}_{ij}^*\right] - \frac{\partial}{\partial x_j}\left[\frac{5}{3}\left(\bar{\mu}\widetilde{u_j \frac{\partial u_k}{\partial x_k}} - \bar{\mu}\tilde{u}_j \frac{\partial \tilde{u}_k}{\partial \tilde{x}_k}\right)\right] \\ &+ \frac{\partial}{\partial x_j}\left[\tau_{ij}\tilde{u}_i + \bar{\mu}\frac{\partial k}{\partial x_j} + \bar{\mu}\frac{\partial}{\partial x_i}\left(\frac{\tau_{ij}}{\bar{\rho}}\right) + R q_j\right] - \frac{\partial}{\partial x_j}\left[\frac{1}{2}\bar{\rho}(\widetilde{u_i u_i u_j} - \widetilde{u_i u_i}\tilde{u}_j)\right] \\ &+ \left(\overline{p\frac{\partial u_k}{\partial x_k}} - \bar{p}\frac{\partial \tilde{u}_k}{\partial x_k}\right),\end{aligned} \tag{3.2}$$

where k, τ_{ij} and q_j are the SGS kinetic energy, SGS stress and SGS heat flux defined by (2.16), (2.12) and (2.13), respectively. R is the specific gas constant,

https://doi.org/10.1017/jfm.2012.115 Published online by Cambridge University Press

with $R = C_p - C_v$, and $D^*_{ij} = D_{ij} - \frac{1}{3}\delta_{ij}D_{kk}$ is the traceless velocity gradient tensor, where $D_{ij} = \partial u_i/\partial x_j$. Equation (3.2) is the exact form of the SGS kinetic energy equation. No additional assumption has been made beyond those in the derivation of the filtered Navier–Stokes equations. For convenience, the following notation is used:

$$f_j = \tfrac{1}{2}\bar{\rho}(\widetilde{u_i u_i u_j} - \widetilde{u_i u_i}\tilde{u}_j), \tag{3.3}$$

$$\epsilon_s = 2\bar{\mu}\left[\widetilde{S^*_{ij}D^*_{ij}} - \widetilde{S}^*_{ij}\widetilde{D^*_{ij}}\right], \tag{3.4}$$

$$\epsilon_c = \frac{\partial}{\partial x_j}\left[\frac{5}{3}\left(\bar{\mu}\,\widetilde{u_j\frac{\partial u_k}{\partial x_k}} - \bar{\mu}\tilde{u}_j\frac{\partial \tilde{u}_k}{\partial \tilde{x}_k}\right)\right], \tag{3.5}$$

$$\Pi = \overline{p\frac{\partial u_k}{\partial x_k}} - \bar{p}\frac{\partial \tilde{u}_k}{\partial x_k}. \tag{3.6}$$

The SGS kinetic energy equation (3.2) reduces to

$$\frac{\partial \bar{\rho}k}{\partial t} = -\frac{\partial \bar{\rho}k\tilde{u}_j}{\partial x_j} - \tau_{ij}\widetilde{S}_{ij} - \epsilon_s - \epsilon_c - \frac{\partial f_j}{\partial x_j} + \Pi + \frac{\partial}{\partial x_j}\left[\tau_{ij}\tilde{u}_i + \bar{\mu}\frac{\partial k}{\partial x_j} + \bar{\mu}\frac{\partial}{\partial x_i}\left(\frac{\tau_{ij}}{\bar{\rho}}\right) + Rq_j\right]. \tag{3.7}$$

In (3.7), $-\partial\bar{\rho}k\tilde{u}_j/\partial x_j$ is the convection term, $-\tau_{ij}\widetilde{S}_{ij}$ is the production term, which is termed the SGS dissipation for the resolved kinetic energy (Piomelli *et al.* 1991) and represents the interscale energy transfer associated with the interaction of the resolved and unresolved scales, $-\epsilon_s$ is the solenoidal dissipation, $-\epsilon_c$ is the dilatational dissipation, f_j is the triple correlation term, Π is pressure dilatation, and the rest are diffusion terms. Note that the dilatational dissipation term is expanded to yield the approximation:

$$\epsilon_c \approx \frac{5}{3}\left[\bar{\mu}\left(\widetilde{\frac{\partial u_k}{\partial x_k}}\right)^2 - \bar{\mu}\left(\frac{\partial \tilde{u}_k}{\partial x_k}\right)^2\right]. \tag{3.8}$$

In (3.7), the SGS stress τ_{ij} and SGS heat flux q_j are modelled in the filtered Navier–Stokes equations (2.6) and (2.7), and the terms ϵ_s, ϵ_c, f_j and Π are to be modelled for the SGS kinetic energy equation.

Note that, when the compressibility becomes negligible, ϵ_c and Π approach zero, Rq_j reduces to $\overline{u_j(\partial p/\partial x_j)} - \tilde{u}_j\overline{(\partial p/\partial x_j)}$ and $-\epsilon_s + (\partial/\partial x_j)[\bar{\mu}(\partial/\partial x_i)(\tau_{ij}/\bar{\rho})]$ yields $-\bar{\mu}[\widetilde{(\partial u_i/\partial x_j)(\partial u_i/\partial x_j)} - (\partial\tilde{u}_i/\partial x_j)(\partial\tilde{u}_i/\partial x_j)]$. Consequently, in the incompressible limit, (3.2) reduces to

$$\frac{\partial \bar{\rho}k}{\partial t} = -\frac{\partial \bar{\rho}k\tilde{u}_j}{\partial x_j} - \tau_{ij}\widetilde{S}_{ij} - \bar{\mu}\left(\widetilde{\frac{\partial u_i}{\partial x_j}\frac{\partial u_i}{\partial x_j}} - \frac{\partial \tilde{u}_i}{\partial x_j}\frac{\partial \tilde{u}_i}{\partial x_j}\right) - \left(\overline{u_j\frac{\partial p}{\partial x_j}} - \tilde{u}_j\overline{\frac{\partial p}{\partial x_j}}\right) + \frac{\partial(\tau_{ij}\tilde{u}_i)}{\partial x_j} + \frac{\partial}{\partial x_j}\left[\bar{\mu}\frac{\partial k}{\partial x_j}\right] - \frac{\partial}{\partial x_j}\left[\frac{1}{2}\bar{\rho}(\widetilde{u_i u_i u_j} - \widetilde{u_i u_i}\tilde{u}_j)\right], \tag{3.9}$$

which is the SGS kinetic energy equation for incompressible flows (Lilly 1967; Schumann 1975) after dividing by ρ on both sides.

https://doi.org/10.1017/jfm.2012.115 Published online by Cambridge University Press

3.2. *Residual term H in the filtered total energy equation*

In most of the LES modelling of compressible flows (e.g. Moin *et al.* 1991; Dubois, Domaradzki & Honein 2002), the residual term H in the filtered energy equation (2.7) is neglected, partially because there are too many unclosed terms in H adding to the complexity of modelling. However, for the proposed dynamic k-equation model, we can take into account all of the terms in H without adding extra computation and modelling cost. Recall the expression for H in equation (2.15):

$$H = -\frac{\partial}{\partial x_j}\left[\frac{1}{2}(\widetilde{\bar{\rho}u_i u_i u_j} - \bar{\rho}\widetilde{u_i u_i}\tilde{u}_j)\right] - \frac{\partial}{\partial x_j}\left[\frac{5}{3}\left(\bar{\mu}\,\widetilde{u_j\frac{\partial u_k}{\partial x_k}} - \bar{\mu}\tilde{u}_j\frac{\partial \tilde{u}_k}{\partial \tilde{x}_k}\right)\right] + \frac{\partial}{\partial x_j}\left[\bar{\mu}\frac{\partial k}{\partial x_j}\right] + \frac{\partial}{\partial x_j}\left[\bar{\mu}\frac{\partial}{\partial x_i}\left(\frac{\tau_{ij}}{\bar{\rho}}\right)\right]. \tag{3.10}$$

Compared with (3.2), all the terms of H reappear in the SGS kinetic energy transport equation. Therefore, the complete filtered total energy equation will be automatically closed once the SGS kinetic energy equation is modelled. Using the same notation as in the SGS kinetic energy equation (3.7), the filtered total energy equation can be rewritten as

$$\frac{\partial}{\partial t}(\bar{\rho}\widetilde{E}) = -\frac{\partial}{\partial x_j}(\bar{\rho}\widetilde{E}\widetilde{u}_j + \bar{p}\widetilde{u}_j - \widetilde{\sigma}_{ij}\widetilde{u}_i - \overline{Q_j} + C_p q_j) + \frac{\partial}{\partial x_j}\left[\tilde{\mu}\frac{\partial k}{\partial x_j}\right] + \frac{\partial}{\partial x_j}\left[\bar{\mu}\frac{\partial}{\partial x_i}\left(\frac{\tau_{ij}}{\bar{\rho}}\right)\right] - \frac{\partial f_j}{\partial x_j} - \epsilon_c. \tag{3.11}$$

3.3. *SGS modelling*

Similar to the compressible DSM, eddy viscosity and eddy diffusivity models are used for the SGS stress τ_{ij} and the SGS heat flux q_j, respectively. However, with the SGS kinetic energy equation, $\sqrt{k}$ is chosen as the velocity scale instead of $\Delta|\widetilde{S}|$, i.e.

$$\tau_{ij} - \tfrac{2}{3}\bar{\rho}k\delta_{ij} = -2C_s\Delta\bar{\rho}\sqrt{k}\widetilde{S}^*_{ij}, \tag{3.12}$$

$$q_j = -\frac{\mu_t}{Pr_t}\frac{\partial \widetilde{T}}{\partial x_j} = -\frac{C_s\Delta\bar{\rho}\sqrt{k}}{Pr_t}\frac{\partial \widetilde{T}}{\partial x_j}. \tag{3.13}$$

Here, $\mu_t = C_s\Delta\bar{\rho}\sqrt{k}$ is the eddy viscosity, and C_s and Pr_t are the model coefficients to be determined dynamically by Germano identity. For convenience, we define the 'eddy conductivity', $\kappa_t = C_p\mu_t/Pr_t$, which will be compared with the thermal conductivity in a later section. The closure of energy equations requires models for f_j, ϵ_s, ϵ_c and Π. We propose the following models for these terms:

$$f_j = C_f\bar{\rho}\Delta\sqrt{k}\frac{\partial k}{\partial x_j}, \tag{3.14}$$

$$\epsilon_s = C_{\epsilon s}\bar{\rho}k^{3/2}\Delta^{-1}, \tag{3.15}$$

$$\epsilon_c = C_{\epsilon c}M_t^2\bar{\rho}k^{3/2}\Delta^{-1}, \tag{3.16}$$

$$\Pi = C_\Pi\Delta^2\frac{\partial\bar{p}}{\partial x_j}\frac{\partial^2\widetilde{u}_k}{\partial x_j\partial x_k}, \tag{3.17}$$

where C_f, $C_{\epsilon s}$, $C_{\epsilon c}$ and C_Π are closure coefficients, Δ is the nominal filter width and $M_t = \sqrt{2k}/a$ is the SGS turbulent Mach number, where a is the mean speed of

https://doi.org/10.1017/jfm.2012.115 Published online by Cambridge University Press

sound. Models for f_j and ϵ_s are adapted from the models of corresponding terms for incompressible Reynolds averaged Navier–Stokes (RANS) equations (Speziale 1991). The model for the dilatational dissipation term ϵ_c is taken from Sarkar *et al.* (1991), and the model for the pressure dilatational term Π is based on a series expansion. For any term that has the structure of $\overline{fg} - \bar{f}\bar{g}$, Bedford & Yeo (1993) show that

$$\overline{fg} - \bar{f}\bar{g} = 2\alpha \frac{\partial \bar{f}}{\partial x_k}\frac{\partial \bar{g}}{\partial x_k} + \frac{1}{2!}(2\alpha)^2 \frac{\partial^2 \bar{f}}{\partial x_k \partial x_l}\frac{\partial^2 \bar{g}}{\partial x_k \partial x_l} + \frac{1}{3!}(2\alpha)^2 \frac{\partial^3 \bar{f}}{\partial x_k \partial x_l \partial x_m}\frac{\partial^2 \bar{g}}{\partial x_k \partial x_l \partial x_m} + \cdots, \tag{3.18}$$

where

$$\alpha(y) = \int_{-\infty}^{\infty} x^2 G(x, y)\, \mathrm{d}x \tag{3.19}$$

and $G(x, y)$ is the kernel of the filter. For a box filter, $\alpha = \Delta^2/24$. In practice, α is approximated by $\alpha = C\Delta^2$, and C is absorbed in the model coefficient C_Π.

Most of the model coefficients can be dynamically computed through the Germano identity. However, since the model for solenoidal dissipation ϵ_s does not scale well across filters (e.g. Pomraning & Rutland 2002), the Germano identity for ϵ_s yields very small values of $C_{\epsilon s}$, which considerably under-predicts the magnitude of ϵ_s (Park & Mahesh 2007), causing incorrect evolution of the SGS kinetic energy. Being modelled similarly, ϵ_c suffers from the same problem, and gives insufficient dissipation to the SGS kinetic energy after the shock, which further affects the resolved quantities through the total energy equation (§ 6). To circumvent this problem, instead of using the Germano identity, which assumes the similarity of SGS stresses between the grid filter level and the test filter level, we use the analogy between the grid-filter-level SGS stress and the Leonard stress L across the test filter level, as used by Menon & Kim (1996). Specifically, as stated in § 2.2, in the Germano identity, for any terms that are of the form $a = \overline{\alpha\beta} - \bar{\alpha}\bar{\beta}$ and modelled as $a = C\,m$, it is assumed that, on the test filter level, $A = \widehat{\overline{\alpha\beta}} - \widehat{\bar{\alpha}}\widehat{\bar{\beta}} = C\,M$ holds. Thus the model coefficient C can be solved by the equation

$$L = \widehat{\bar{\alpha}\bar{\beta}} - \widehat{\bar{\alpha}}\widehat{\bar{\beta}} = C(M - \hat{m}), \tag{3.20}$$

where L is the Leonard stress term. In contrast, Menon & Kim (1996) assume that, on the test filter level,

$$A = \widehat{\bar{\alpha}\bar{\beta}} - \widehat{\bar{\alpha}}\widehat{\bar{\beta}} = C\,M, \tag{3.21}$$

from which the model coefficient C is directly solvable. Applying this methodology to ϵ_s and ϵ_c, the resulting equations for $C_{\epsilon s}$ and $C_{\epsilon c}$ are

$$2\left[\widehat{\bar{\mu}\widetilde{D}^*_{ij}\widetilde{S}^*_{ij}} - \widehat{\bar{\mu}}\widehat{\widetilde{D}^*_{ij}}\widehat{\widetilde{S}^*_{ij}}\right] = C_{\epsilon s}\widehat{\bar{\rho}}K^{3/2}\widehat{\Delta}^{-1} \tag{3.22}$$

and

$$\frac{5}{3}\left[\widehat{\bar{\mu}\left(\frac{\partial \widetilde{u}_k}{\partial x_k}\right)^2} - \widehat{\bar{\mu}}\left(\frac{\partial \widehat{\widetilde{u}_k}}{\partial x_k}\right)^2\right] = 2C_{\epsilon c}\frac{\widehat{\bar{\rho}}^2}{\gamma \widehat{\bar{p}}}K^{5/2}\widehat{\Delta}^{-1}, \tag{3.23}$$

https://doi.org/10.1017/jfm.2012.115 Published online by Cambridge University Press

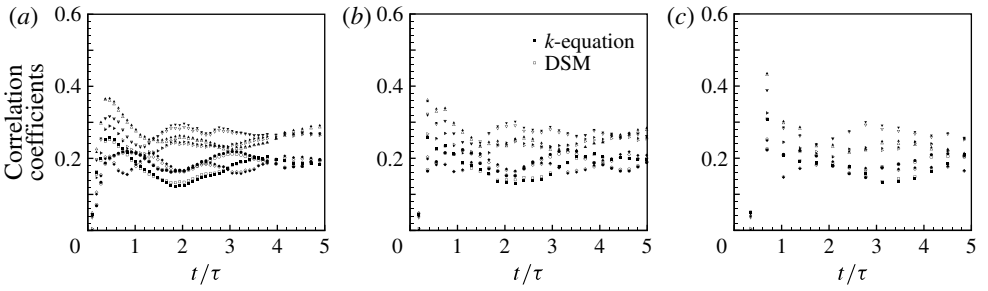


FIGURE 1. Correlation coefficients for SGS stresses τ_{ij} for the three cases (*a*) $M_t = 0.2$, (*b*) $M_t = 0.4$ and (*c*) $M_t = 0.6$: τ_{11}, square; τ_{12}, delta; τ_{13}, right-triangle; τ_{22}, diamond; τ_{23}, gradient; and τ_{33}, circle. Filled symbols, *k*-equation model; hollow symbols, DSM.

where K is the 'sub-test-filter scale' kinetic energy and is of the form

$$K = \widehat{k} + \tfrac{1}{2}(\widehat{\widetilde{u}_i\widetilde{u}_i} - \widehat{\widetilde{u}}_i\widehat{\widetilde{u}}_i). \tag{3.24}$$

Equations (3.22) and (3.23) yield reasonable values of $C_{\epsilon s}$ and $C_{\epsilon c}$, which appear to give the correct decay rate of the SGS kinetic energy of temporal decaying isotropic turbulence and reasonable evolution of the SGS kinetic energy across shocks. Note that this method is only applied to the determination of $C_{\epsilon s}$ and $C_{\epsilon c}$, and the Germano identity is used everywhere else.

4. *A priori* tests

This section presents *a priori* tests for the SGS models using DNS results of temporal decaying isotropic turbulence. The DNS employed a pseudo-spectral Fourier collocation scheme for spatial discretization and a fourth-order Runge–Kutta method for time advancement. The skew-symmetric form of the convection terms is used to suppress aliasing errors. Details and validation of the numerical method are discussed by Ghosh & Mahesh (2008). The initial three-dimensional energy spectrum is

$$E(k) = \frac{16}{3}\sqrt{\frac{\pi}{2}}\frac{M_t^2}{k_0}\left(\frac{k}{k_0}\right)^4 \exp\left(\frac{-2k^2}{k_0^2}\right), \tag{4.1}$$

where $k_0 = 4$. This energy spectrum gives an initial root mean square (r.m.s.) velocity fluctuation of $u_{rms} = M_t/\sqrt{3}$, initial Taylor microscale of $\lambda_0 = 2/k_0$, and thus eddy turnover time of $\tau = u_{rms}/\lambda_0 = 2\sqrt{3}/(k_0 M_t)$. Three cases are considered here, which have initial turbulent Mach numbers of $M_t = 0.2$, 0.4 and 0.6, respectively. The initial Taylor microscale Reynolds number is set as $Re_\lambda = u_{rms}\lambda_0/\nu = 67.6$ for all cases. The simulations are performed on a $2\pi^3$ cubical domain with 256^3 control volumes. The grid resolution is doubled in each direction compared to the corresponding simulations of Spyropoulos & Blaisdell (1996) under similar flow conditions. The DNS data are filtered onto a 32^3 grid, and correlation coefficients between the exact SGS terms and their modelled values are computed. Here, the box filter is used, since it has a positive definite kernel that allows positive SGS kinetic energy to be obtained (Vreman *et al.* 1995). Figures 1 and 2 show the correlation coefficients over time between the exact SGS stress components, SGS heat flux components and their models, respectively. The DSM (equations (2.19) and (2.20), denoted by hollow symbols) and the *k*-equation model (equations (3.12) and (3.13), denoted by filled symbols) are compared as well.

https://doi.org/10.1017/jfm.2012.115 Published online by Cambridge University Press

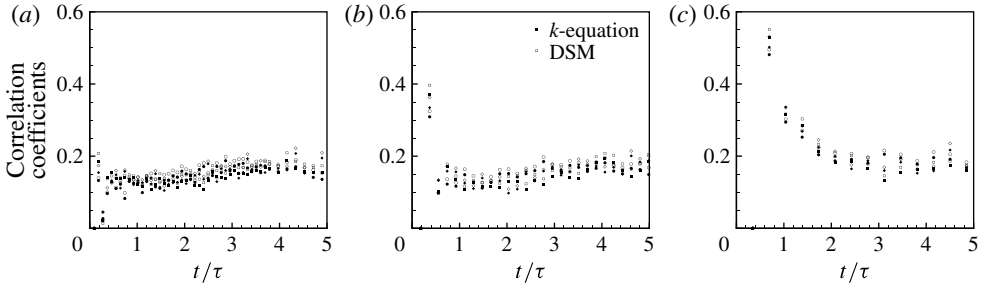


FIGURE 2. Correlation coefficients for SGS heat flux q_j for the three cases (*a*) $M_t = 0.2$, (*b*) $M_t = 0.4$ and (*c*) $M_t = 0.6$: q_1, square; q_2, diamond; and q_3, circle.

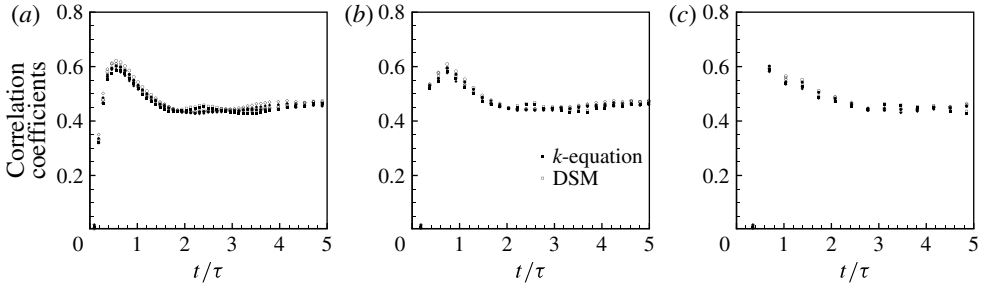


FIGURE 3. Correlation coefficients for $\partial\tau_{ij}/\partial x_j$ for the three cases (*a*) $M_t = 0.2$, (*b*) $M_t = 0.4$ and (*c*) $M_t = 0.6$: $\partial\tau_{1j}/\partial x_j$, square; $\partial\tau_{2j}/\partial x_j$, diamond; and $\partial\tau_{3j}/\partial x_j$, circle.

For all cases and all components of the SGS stress and SGS heat flux, the DSM and the *k*-equation model yield very similar levels of correlation, which is known to be low for the Smagorinsky model. The shear stresses are observed to correlate better than normal stresses (figure 1). As shown in figure 2, the correlation coefficients for SGS heat flux appear to be higher in the highly compressible case ($M_t = 0.6$) than in the other two cases ($M_t = 0.2$ and $M_t = 0.4$). Figures 3 and 4(*a*) show the correlation coefficients for the divergence of SGS stress and that of SGS heat flux. These divergence terms are more important, because the SGS stress and heat flux appear in the form of divergence in the momentum and energy equations. These figures show that the divergence of these modelled terms have better correlation than their components. Again, the *k*-equation model and DSM give very similar correlation levels in $\partial\tau_{ij}/\partial x_j$, while the correlation coefficients for $\partial q_j/\partial x_j$ in the *k*-equation model are a little smaller than, but still comparable to, those in the DSM. The correlations for ϵ_s, ϵ_c and Π are shown in figure 4(*b*). It is encouraging that the proposed model for pressure dilatation Π (equation (3.17)) correlates very well with the actual values at all three turbulent Mach numbers. The model for ϵ_s also correlates reasonably well with its actual value, and the correlation coefficients are the second largest among all the SGS terms. For the dilatational dissipation ϵ_c, the correlation coefficients are comparable to those for τ_{ij} and q_j. The correlation for the triple product term is found to be the lowest (not shown). Among all the correlations, it also appears that only quantities related to SGS heat flux (figures 2 and 4*a*) show discernible Mach number dependence. As noted in numerous studies (e.g. Meneveau 1994; Vreman *et al.*

https://doi.org/10.1017/jfm.2012.115 Published online by Cambridge University Press

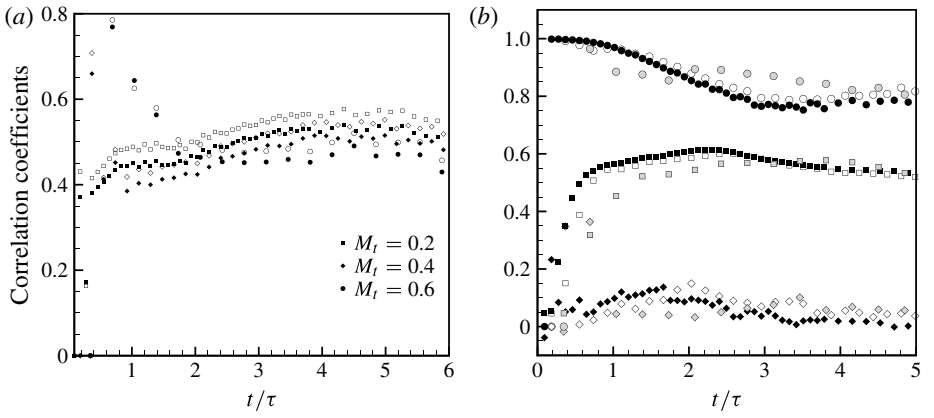


FIGURE 4. (*a*) Correlation coefficients for $\partial q_j/\partial x_j$: k-equation model (filled symbols) and DSM (hollow symbols). (*b*) Correlation coefficients for ϵ_s (square), ϵ_c (diamond) and Π (circle).

1995), *a priori* tests of SGS models are certainly of some value, but need careful interpretation. In order to draw conclusions about the performance of SGS models, *a posteriori* tests are performed in the next section.

5. *A posteriori* tests

5.1. *Numerical algorithm*

The numerical scheme is that developed by Park & Mahesh (2007) for solving the compressible Navier–Stokes equations (2.5)–(2.8) on unstructured grids. The governing equations are discretized using a cell-centred finite volume scheme. Upon integration over the control volume (CV), application of the Gauss theorem and some rearrangement, the governing equations may be written as

$$\left.\begin{aligned}
\frac{\partial \rho_{cv}}{\partial t} &= -\frac{1}{V_{cv}} \sum_{faces} \rho_f v_N A_f, \\
\frac{\partial \left(\rho u_i\right)_{cv}}{\partial t} &= -\frac{1}{V_{cv}} \sum_{faces} [(\rho u_i)_f \, v_N + p_f n_i - \sigma_{ik,f} n_k] A_f, \\
\frac{\partial \left(E_T\right)_{cv}}{\partial t} &= -\frac{1}{V_{cv}} \sum_{faces} [(E_T + p)_f \, v_N - \sigma_{ik,f} u_{i,f} n_k - Q_{k,f} n_k] A_f,
\end{aligned}\right\} \tag{5.1}$$

where V_{cv} is the volume of CV, A_f is the area of face, n_i is the outward normal vector at the surface and v_N is the face-normal velocity. The solution is advanced in time using a second-order explicit Adams–Bashforth scheme.

Discretization of the governing equations involves reconstruction of the variables at the faces from the CV centre values. Also, the spatial accuracy of the algorithm is sensitive to this flux reconstruction. The simulations employ a modified least-squares method (MLSQ; Park & Mahesh 2007) for this reconstruction, the modified wavenumber of which shows better spectral resolution than the fourth-order central difference scheme, at high wavenumbers. When tested on vortex convection, the Taylor–Green problem, decaying isotropic turbulence and scalar convection, the MLSQ method is found to be more accurate than a simple symmetric reconstruction, and

https://doi.org/10.1017/jfm.2012.115 Published online by Cambridge University Press

more stable than a least-squares reconstruction. The viscous stress term is split into two parts, i.e. $\sigma_{ij} = \sigma_{ij}^s + \sigma_{ij}^c$, where $\sigma_{ij}^s = (\mu/Re)(\partial u_i/\partial x_j)$ is the incompressible part and $\sigma_{ij}^c = (\mu/Re)[(\partial u_j/\partial x_i) - \frac{2}{3}(\partial u_k/\partial x_k)\delta_{ij}]$ is the compressible part. Such splitting ensures that the dominant incompressible component only depends on the nearest neighbours and is therefore more accurate at high wavenumbers, and devoid of odd–even decoupling.

The algorithm uses a shock-capturing scheme that was originally proposed by Yee, Sandham & Djomehri (1999) for structured meshes and was extended by Park & Mahesh (2007) to unstructured meshes, and further localized to reduce unnecessary numerical dissipation. The shock capturing is implemented in predictor–corrector form. Once the predicted solution $\hat{\boldsymbol{q}}^{n+1}$ is obtained from $\boldsymbol{q}^n$, the final solution $\boldsymbol{q}^{n+1}$ at $t + \Delta t$ is determined from a corrector step:

$$\boldsymbol{q}_{cv}^{n+1} = \hat{\boldsymbol{q}}_{cv}^{n+1} - \frac{\Delta t}{V_{cv}} \sum_{faces} (\boldsymbol{F}_f^* \cdot \boldsymbol{n}_f) A_f, \tag{5.2}$$

where $\boldsymbol{F}_f^*$ is the filter numerical flux. Here, $\boldsymbol{q}^n$ and $\boldsymbol{q}^{n+1}$ are the conserved variable arrays at time step n and $n+1$, and $\hat{\boldsymbol{q}}^{n+1}$ is the set of variables at time step $n+1$ but prior to the application of shock capturing. The predictor step (base scheme) is symmetric and non-dissipative, and is designed to represent accurately broadband turbulence, whereas the corrector step is a characteristic-based filter that is active only in the vicinity of discontinuities. Therefore, the overall scheme avoids unnecessary numerical dissipation.

The algorithm was evaluated by Park & Mahesh (2007) for shock–vortex interaction, shock tube problems, a two-dimensional mixing layer and under-resolved turbulence. For shock–vortex interaction, the algorithm captures the deformation of the vortex and shock wave accurately. In the mixing layer problem, the formation of shocklets as well as vortex pairing and merging are well represented. Importantly, it is observed that any numerical dissipation is localized to the immediate vicinity of the discontinuity, and the solution away from the shock sees zero numerical dissipation. When applied to an under-resolved turbulence problem, the algorithm shows minimal effects of numerical dissipation when the shock-capturing scheme is turned on and off. Moreover, the algorithm is found to work well even on tetrahedral meshes for all the test problems, and shocks are captured within two grid points in spite of coarse resolution. Further details about the algorithm are provided in Park & Mahesh (2007). The algorithm has also been successfully applied to various flows with complex geometries such as roughness-induced transition in supersonic boundary layers (Muppidi & Mahesh 2011) and simulations of high-speed jets in cross-flow (Chai & Mahesh 2011).

The proposed dynamic k-equation model is incorporated into the above numerical scheme and applied to decaying isotropic turbulence and normal shock–isotropic turbulence interaction for evaluation.

5.2. *Decaying isotropic turbulence*

Two cases are considered here. One is a nearly incompressible simulation that is compared to the experiment of Comte-Bellot & Corrsin (1971), and the other is a compressible simulation where the filtered DNS results in § 4 are used for validation. Also compared are LES results using the DSM. All of the large-eddy simulations are performed on a 32^3 periodic cubical domain, and spatial averaging over homogeneous directions is applied during the dynamic procedures.

https://doi.org/10.1017/jfm.2012.115 Published online by Cambridge University Press

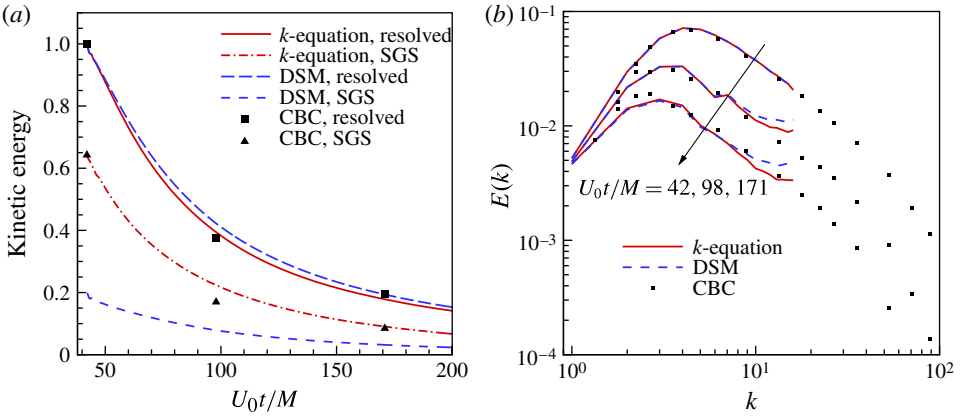


FIGURE 5. (Colour online available at journals.cambridge.org/flm) LES of the CBC decaying isotropic turbulence on 32^3 resolution. (*a*) Kinetic energy decay; (*b*) energy spectra.

5.2.1. *Quasi-incompressible simulation*

The experiment of Comte-Bellot & Corrsin (1971, CBC) is simulated as temporally decaying isotropic turbulence through time–space correlation. The initial energy spectrum is obtained from the experiment at non-dimensional time $U_0t/M = 42$. Initially, the velocity field is purely solenoidal, while the pressure field is computed from the incompressible Poisson equation. The density is assumed to be uniform, so the initial temperature field has a similar spectrum as pressure due to the equation of state. The SGS kinetic energy is initialized using Yoshizawa's model, but its magnitude is scaled up so that the mean value of the SGS kinetic energy matches the experimental SGS kinetic energy, which can be estimated by integrating the energy spectrum over wavenumbers that are higher than the cutoff wavenumber. Figure 5(*a*) shows the temporal decay of kinetic energy, while figure 5(*b*) shows the energy spectra at different time instants $U_0t/M = 42$, 98 and 171 during the CBC experiment. The DSM results under the same conditions are shown for comparison. As shown in figure 5(*a*), the results from the dynamic k-equation model are very encouraging in that both decay of resolved kinetic energy and SGS kinetic energy agree well with the experiment. Yoshizawa's model used in DSM under-predicts the SGS kinetic energy. Figure 5(*b*) shows that the energy spectra predicted by the k-equation model agree better with the experiments, and less energy is piled up at higher wavenumbers compared with the DSM results.

Figure 6 shows the effects of initial SGS kinetic energy. Figure 6(*a*) shows that the initial decay rate of resolved kinetic energy is slightly smaller when a lower value of initial SGS kinetic energy is specified, since the eddy viscosity is proportional to $\sqrt{k}$ (equation (3.12)). But this influence is small over a wide range of initial k, so that the k-equation model has the potential to yield a reasonable prediction when the SGS kinetic energy is not accurate. Note that, even with the very small magnitude of initial k, the proposed k-equation model gives a prediction for the resolved energy decay that is comparable to that of the DSM. Also, the SGS kinetic energy always recovers to its 'correct' value as flow evolves. From figure 6(*b*), it seems that the effect of initial SGS kinetic energy only shows up at high wavenumbers, where the energy cusp is smaller than or comparable to the DSM results. Figure 6 also suggests that $\frac{1}{2}(\widetilde{\widetilde{u}_i\widetilde{u}_i} - \widehat{\widetilde{u}_i}\widehat{\widetilde{u}_i})$ (scale

https://doi.org/10.1017/jfm.2012.115 Published online by Cambridge University Press

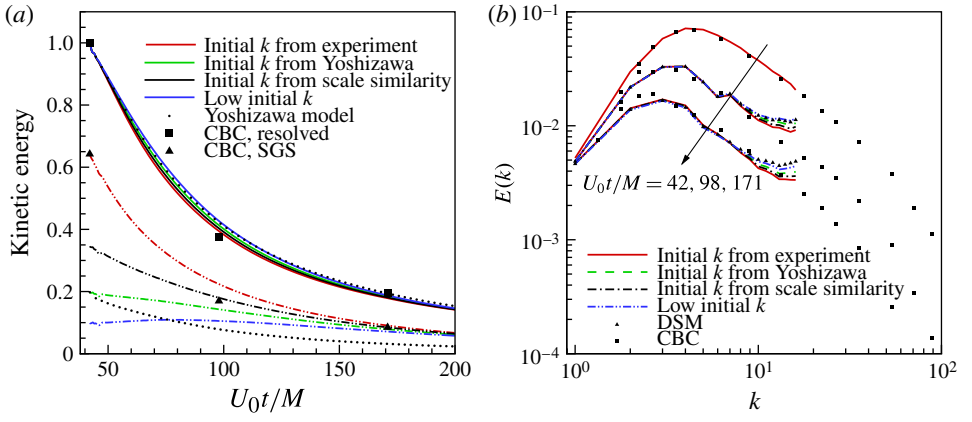


FIGURE 6. (Colour online) Effect of initial SGS kinetic energy. (*a*) Kinetic energy decay: solid curves, resolved kinetic energy; other non-solid curves, SGS kinetic energy; (*b*) energy spectra.

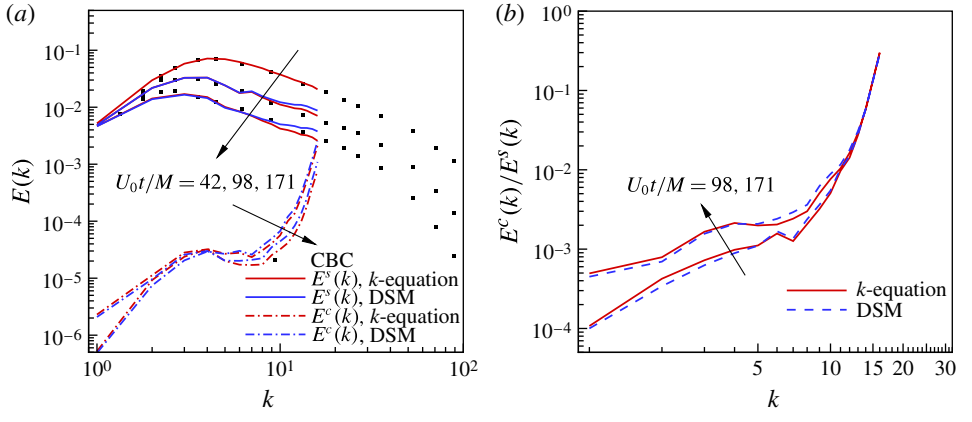


FIGURE 7. (Colour online) (*a*) Decomposition of three-dimensional energy spectra. (*b*) Ratio of compressible energy spectra to solenoidal part; k is initialized with experimental condition in k-equation model.

similarity) is a good estimation of the initial SGS kinetic energy if the actual value is unknown.

Energy cusps are observed in the energy spectra shown in figures 5(*b*) and 6(*b*). Decomposing the energy spectra into a compressible part $E^c(k)$ and a solenoidal part $E^s(k)$ (Erlebacher *et al.* 1990), as shown in figure 7(*a*), reveals that the energy cusps are mainly caused by the compressible part of the energy. Because of the periodic boundary conditions, initial acoustic transients will never exit the computational domain, and will steepen up over time. Figure 7(*b*) shows that, at moderate length scales, the solenoidal part of the kinetic energy decays faster than the compressible part, and the ratio of $E^c(k)$ to $E^s(k)$ increases over time. However, the compressible kinetic energy accounts for only around 0.1 % of the solenoidal energy. At high wavenumbers, the ratio of $E^c(k)$ to $E^s(k)$ is up to 30 %, and does not appear to change over time.

https://doi.org/10.1017/jfm.2012.115 Published online by Cambridge University Press

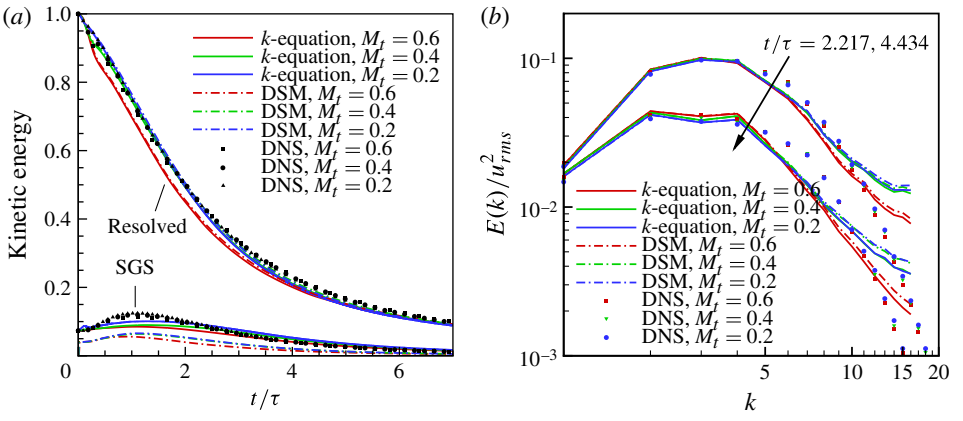


FIGURE 8. (Colour online) Simulations of compressible isotropic turbulence with initial energy spectrum from (4.1): (*a*) time evolutions of kinetic energy; (*b*) energy spectra at two different instants.

5.2.2. *Compressible simulations*

The compressible simulations have the same initial spectra ($\backsim k^4 e^{-k^2}$) as the *a priori* tests in § 4. Three turbulent Mach numbers of $M_t = 0.2$, 0.4 and 0.6 are considered. The initial SGS kinetic energy is derived from the filtered DNS results. Figure 8(*a*) compares the time evolution of the kinetic energy with the filtered DNS results and the DSM results as well. In terms of resolved kinetic energy decay, good agreement can be observed between LES and filtered DNS for the $M_t = 0.2$ and 0.4 cases. The $M_t = 0.6$ case suffers from an initial transient due to 'inconsistent' initial conditions (Ristorcelli & Blaisdell 1997), and is a little off from the DNS results. Figure 8(*b*) shows the energy spectra at times $t/\tau = 2.217$ and 4.434. Consistent with the energy decay shown in figure 8(*a*), the difference in energy spectra between cases $M_t = 0.2$ and 0.4 is very small, while the case $M_t = 0.6$ differs from the others due to initial transients, and the difference is mainly in high wavenumbers. Compared with the DSM results, the k-equation model yields a similar decay of resolved kinetic energy. However, the SGS kinetic energy predicted by the proposed transport equation (equation (3.7)) agrees with the DNS results much better than Yoshizawa's formula in the DSM (figure 8*a*). Consistent with the quasi-incompressible simulation (figure 5), the k-equation model predicted better energy spectra than the DSM at high wavenumbers, as observed in figure 8(*b*). Given that the DSM is known to perform well for decaying isotropic turbulence, the improvement of the proposed dynamic k-equation model is encouraging.

Figure 9(*a*) compares the time evolution of the r.m.s. density fluctuations with the filtered DNS results. Good agreement can be observed for simulations at all three Mach numbers. The simulation results using the k-equation model and DSM are very close. Figure 9(*b*) shows the contours of velocity divergence on the plane $z = 3.83$ for $M_t = 0.6$ at time $t/\tau = 1.0$, along with the in-plane velocity vectors. In the region of peak negative divergence, marked by the white circle, a sudden decrease of normal velocity component is observed. At the upstream CV centre, the Mach number is found to be $M_1 = 1.238$. From the Rankine–Hugoniot relation, the pressure jump ratio for this Mach number is estimated to be $p_2/p_1 = 1.62$. From the simulation, the pressure ratio is found to be $p_2/p_1 = 1.71$, which is very close to the

https://doi.org/10.1017/jfm.2012.115 Published online by Cambridge University Press

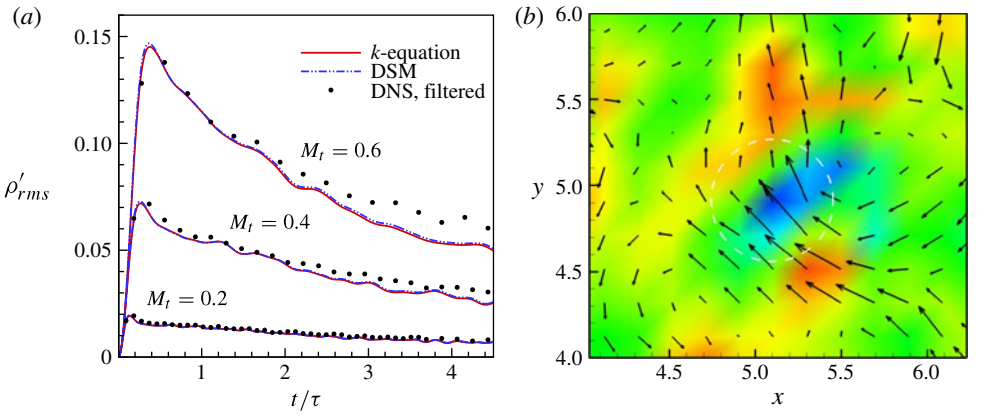


FIGURE 9. (Colour online) (*a*) Time evolutions of r.m.s. density fluctuations; (*b*) divergence contour superimposed with in-plane velocity vectors for the case $M_t = 0.6$ at time $t/\tau = 1.0$.

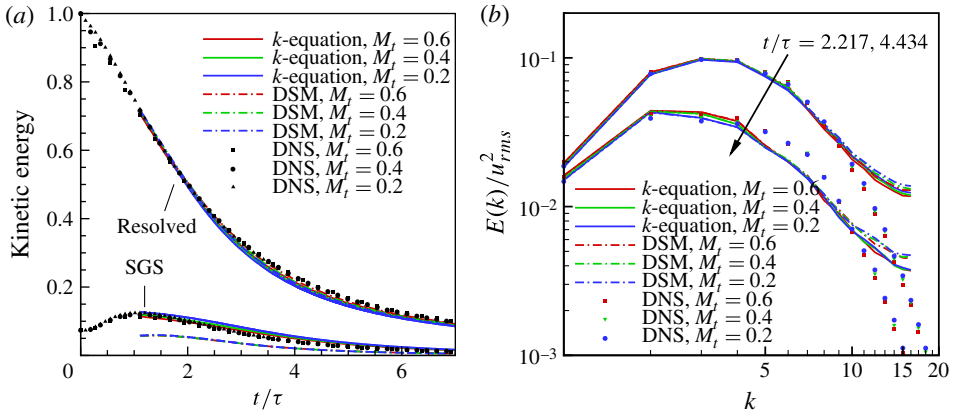


FIGURE 10. (Colour online) Initial condition from filtered DNS at $t/\tau \approx 1.1$: (*a*) time evolutions of kinetic energy; (*b*) energy spectra at two different instants.

Rankine–Hugoniot relation, considering that the flow is not stationary. This ability of the proposed SGS model to model turbulence with highly compressible local regions is encouraging.

To access the effect of initial transients, LES was performed using the filtered DNS field at $t/\tau \approx 1.1$ as the initial condition. Figure 10 shows the kinetic energy decay and energy spectra. As shown in figure 10(*a*), the decay of the resolved kinetic energy in $M_t = 0.6$ is noticeably improved. Moreover, the SGS kinetic energy from the *k*-equation model also achieves better agreement with the DNS, while Yoshizawa's formula in the DSM continues to under-predict the SGS kinetic energy. In figure 10(*b*), the energy spectra for $M_t = 0.6$ collapse with the other two cases after removal of initial transients. Compared with figure 8(*b*), all spectra agree with the DNS better at medium wavenumbers, especially at $t/\tau = 2.217$. The remaining difference between the LES and DNS at high and medium wavenumbers at $t/\tau = 4.434$ is likely to be related to the artificial initial $\backsim k^4 e^{-k^2}$ energy spectra, because good agreement in

https://doi.org/10.1017/jfm.2012.115 Published online by Cambridge University Press

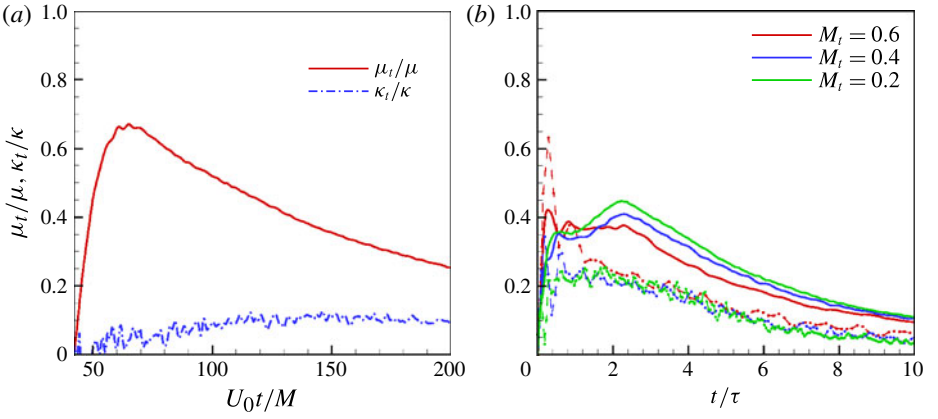


FIGURE 11. (Colour online) Eddy viscosity and conductivity for the decaying isotropic turbulence: (*a*) CBC; (*b*) compressible case, where solid lines are eddy viscosity, symbols on dashed lines are eddy conductivity, and different colours denote different initial M_t.

both kinetic energy decay and spectra is observed in incompressible simulations when physical initial energy spectrum from CBC's experiment is used. Figure 10 also shows that the improvement from the *k*-equation model is consistent, which is independent of the initial conditions.

5.2.3. *Eddy viscosity and 'eddy conductivity'*

Figures 11(*a*) and 11(*b*) show the time evolution of the eddy viscosity and 'eddy conductivity' for quasi-incompressible and fully compressible isotropic turbulence, respectively. For the quasi-incompressible case, the eddy viscosity contributes up to 70 % of the molecular viscosity, and decreases as the turbulence decays. The eddy conductivity is approximately constant as the flow evolves, and its value is only around 10 % of the thermal conductivity. For the highly compressible case, the maximum ratio of eddy viscosity to molecular viscosity is less than, but still comparable to, that in CBC isotropic turbulence, whereas the maximum ratio of eddy conductivity to thermal conductivity is more than twice that for the CBC case. Large initial transients in μ_t/μ and κ_t/κ are observed as the flows adapt to the initial conditions generated by the three-dimensional energy spectrum equation (4.1). It also appears that the eddy viscosity decreases with M_t, while the eddy conductivity increases slightly with M_t.

5.3. *Normal shock–isotropic turbulence interaction*

Shock–turbulence interactions prevail in high-speed turbulent flows. It is necessary for a good compressible SGS model to accurately predict the evolution of the turbulent flow across a normal shock wave. The schematic of the problem is shown in figure 12. Isotropic turbulence is introduced at the inflow, decays spatially over a short distance and then interacts with a statistically stationary normal shock. A sponge layer is used at the end of the computational domain to absorb reflected acoustic oscillations. Spatial averaging over homogeneous directions (*y*–*z* planes) is applied during the dynamic procedures.

Two cases are considered. The first case has low *Re*, which corresponds to the DNS of Mahesh, Lele & Moin (1997), where the inflow Mach number is $M = 1.29$, the turbulent Mach number of the inflow is $M_t = 0.14$ and the microscale Reynolds

https://doi.org/10.1017/jfm.2012.115 Published online by Cambridge University Press

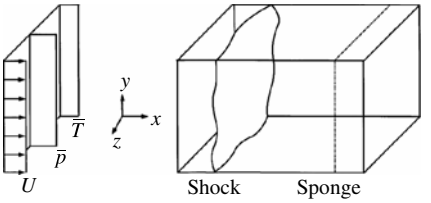


FIGURE 12. Schematic of shock–turbulence interaction problem.

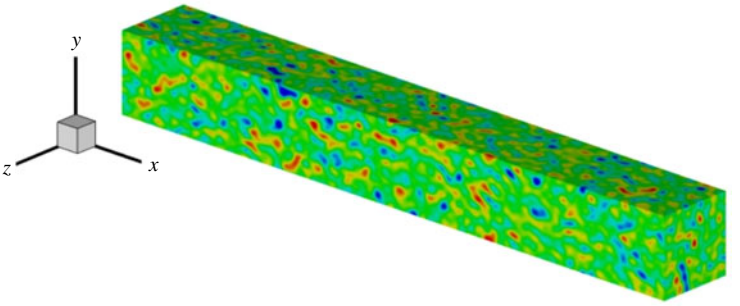


FIGURE 13. (Colour online) Decaying isotropic turbulence in long periodic box.

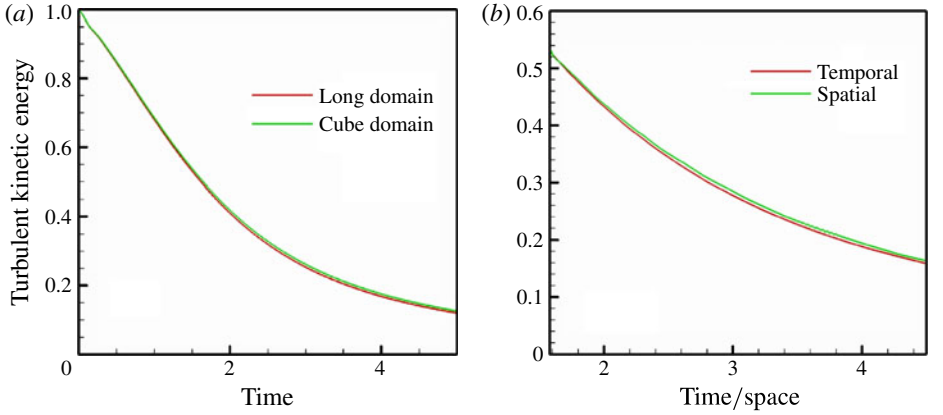


FIGURE 14. (Colour online) Validation of inflow turbulence generation and implementation.

number is $Re_\lambda = 19.1$. The second case corresponds to the DNS of Larsson & Lele (2009), which has higher Re, free stream Mach number M and turbulent Mach number M_t ($M = 1.5$, $M_t = 0.221$ and $Re_\lambda = 40.0$). The two simulations are carried out on the same computational domain with exactly the same mesh. The domain has the dimension of $L_x = 10$ in the streamwise direction, and $L_y = L_z = 2\pi$ in the transverse directions. The mesh has 180×32^2 CVs, which is uniform in the transverse directions and clustered in the vicinity of the shock in the streamwise direction.

The inflow isotropic turbulence is generated using a method similar to Mahesh *et al.*'s (1997) isotropic turbulence, which has the initial energy spectrum of equation

https://doi.org/10.1017/jfm.2012.115 Published online by Cambridge University Press

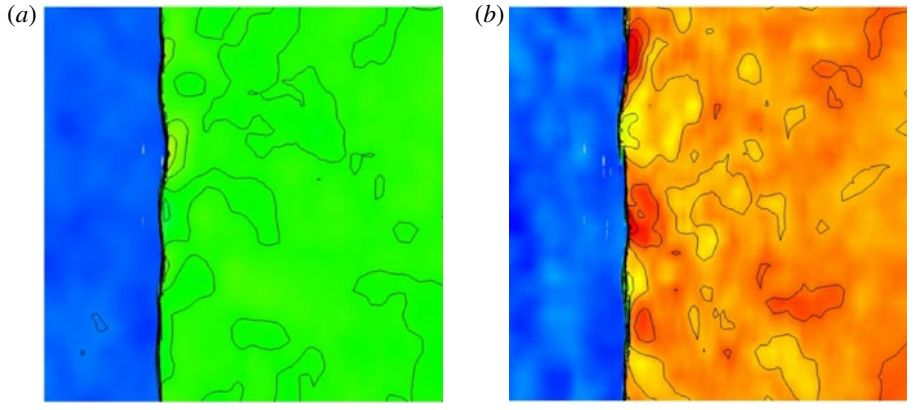


FIGURE 15. (Colour online) Instantaneous density fields superposed by isopressure lines on central plane: (*a*) low *Re*; (*b*) high *Re*.

(4.1) and is allowed to decay temporally until the designated M_t and Re_λ are reached. Then, an instantaneous realization of the flow field is taken and used as the inflow of the shock–turbulence interaction problem using Taylor's hypothesis. Simulation of isotropic turbulence is performed on a uniformly meshed long periodic box, which has the dimension of $n\pi \times 2\pi \times 2\pi$ (figure 13). A large enough value of n is chosen to generate an inflow data sequence that is sufficiently long to provide unduplicated isotropic inflow turbulence for several flow-through times, so that converged statistics can be achieved. For the current case, n is chosen as 16, which will provide around five flow-through times of inflow data and is proven to be enough for the statistics to converge. This methodology is validated by temporally and spatially decaying isotropic turbulence as shown in figure 14. Figure 14(*a*) compares the temporal decay of kinetic energy for isotropic turbulence in a periodic cube and a long periodic box, starting with the same energy spectrum. Figure 14(*b*) compares the energy decay rate of temporally decaying isotropic turbulence and the spatially decaying turbulence, where the inflow isotropic turbulence is extracted from the temporal case at time $t/\tau = 1.58$. Good agreement is observed for both cases. Then, the isotropic turbulent inflow is allowed to convect into the computational domain of shock–turbulence interaction.

5.3.1. *Instantaneous field*

Figure 15 shows instantaneous density contours on the central plane $z = 0$. The overlaid contour lines are isopressure lines that show the shock wave. The upstream turbulence causes the shock front to distort in the transverse (y and z) directions. The distortion is found to be stronger for the high-*Re* and high-M_t case, where the shock front also breaks occasionally. Downstream of the shock, more small-scale flow structures can also be observed for the high-*Re* case.

5.3.2. *Turbulent intensities*

Figure 16 compares the distribution of averaged turbulent intensities calculated from the k-equation model with the DNS (Mahesh *et al.* 1997) and DSM results. The turbulent intensities are normalized by their values immediately upstream of the shock, to compare to the DNS. Good agreement is observed between the k-equation model and the DNS results. Note that the turbulent intensities are very high in the immediate vicinity of the shock wave. This behaviour is due to statistical intermittency associated

https://doi.org/10.1017/jfm.2012.115 Published online by Cambridge University Press

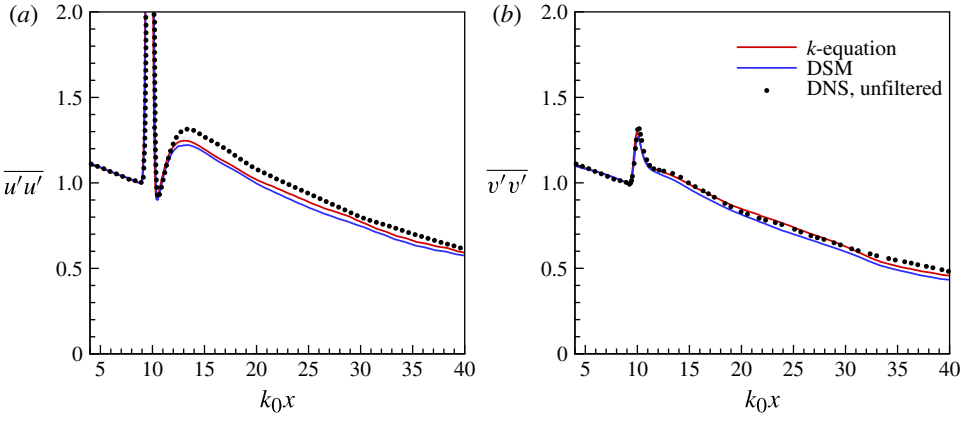


FIGURE 16. (Colour online) Distribution of averaged turbulent intensities for the low-*Re* case.

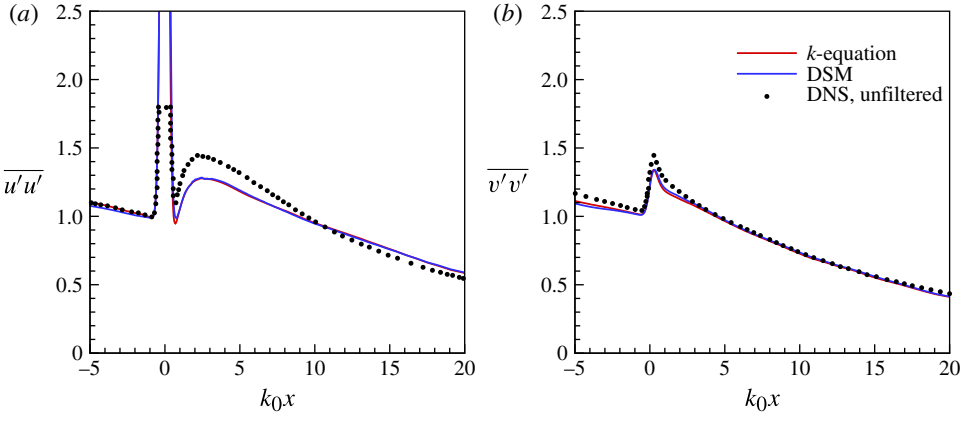


FIGURE 17. (Colour online) Distribution of averaged turbulent intensities for the high-*Re* case. The shock position has been shifted to $x = 0$ for comparison with DNS.

with motions of the shock wave. Owing to shock oscillation, the shock jump would show up as unsteadiness to a fixed probe. Such behaviour is also observed in the DNS of shock–turbulent interaction, where the shock thickness is resolved (Lee, Lele & Moin 1993; Mahesh *et al.* 1997). Figure 17 compares the distribution of averaged turbulent intensities calculated from the *k*-equation model with the DNS and DSM results for the high-*Re* case (Larsson & Lele 2009). All of the curves in figure 17 are normalized by $\overline{u'u'}$ immediately upstream of the shock as in the DNS. Overall, the agreement is reasonable. The *k*-equation model under-predicts the decay rate of $\overline{u'u'}$ far downstream. However, considering that the current LES uses only 1.8×10^5 CVs compared to 1.5×10^8 CVs in the DNS, the agreement is quite good. Note that the DNS inflow is somehow less isotropic than the current LES inflow because of the different inflow generation methodologies. This may be responsible for the small difference between the LES and DNS in $\overline{v'v'}$ at the inflow. Compared with the DSM, $\overline{u'u'}$ predicted by the *k*-equation model is slightly closer to the DNS results for the

https://doi.org/10.1017/jfm.2012.115 Published online by Cambridge University Press

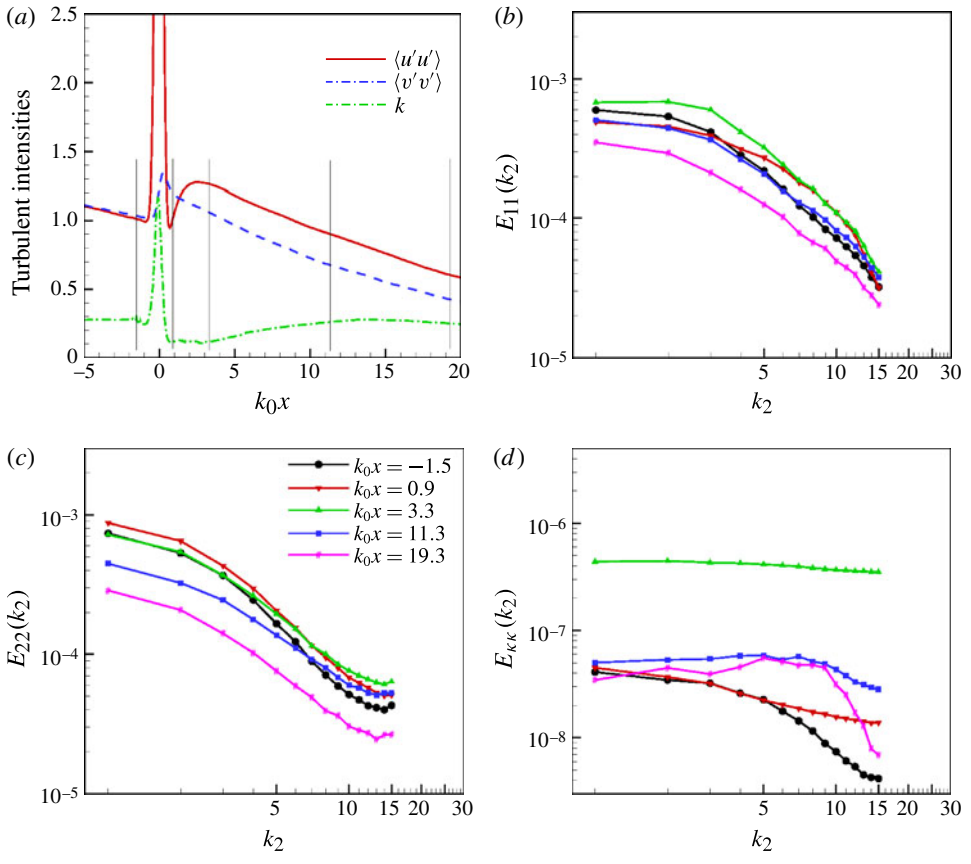


FIGURE 18. (Colour online) (*a*) Evolution of turbulent energies. One-dimensional energy spectra: (*b*) E_{11}, (*c*) E_{22} and (*d*) E_{kk} (energy spectra of SGS kinetic energy).

low-*Re* case (figure 16*a*); while, for the high-*Re* case, the *k*-equation model results are almost identical to those of the DSM (figure 17). This is reasonable, because strong shock and turbulent interaction is dominated by linear effects (Mahesh *et al.* 1997), so that the contribution of SGS models at the shock front is less obvious.

5.3.3. *Energy spectra*

Figure 18 shows one-dimensional energy spectra of velocity components and the SGS kinetic energy at different locations. In the current simulation, the flow is isotropic upstream of the shock and axisymmetric downstream of the shock, so that $E_{22}(k_2) \approx E_{33}(k_2)$; therefore E_{33} is not plotted here. Distribution of SGS kinetic energy k is also plotted in figure 18(*a*), with vertical lines marking the locations where the energy spectra are calculated. As shown, $k_0x = -1.5$ is at the shock upstream; $k_0x = 0.9$ is almost immediately downstream of the shock; $k_0x = 3.3$ is a location near the peak value of $\overline{u'u'}$ at the shock downstream; and $k_0x = 11.3$ and $k_0x = 19.3$ are two locations far downstream.

Note that even the smallest scales have large energy levels. As seen from figure 18(*b*), across the shock (from $k_0x = -1.5$ to $k_0x = 0.9$), the energy spectrum of E_{11} is amplified in medium wavenumbers, decreases in small wavenumbers and is preserved at high wavenumbers. This indicates a decrease of turbulent length scale in

https://doi.org/10.1017/jfm.2012.115 Published online by Cambridge University Press

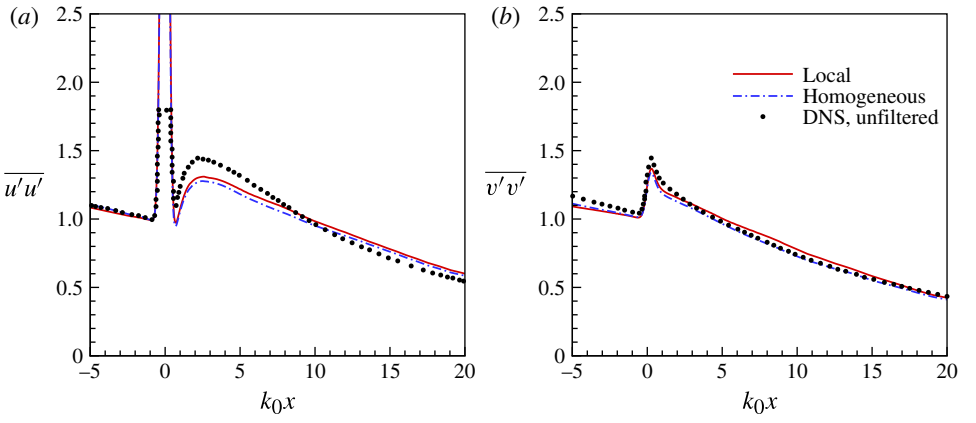


FIGURE 19. (Colour online) Comparison of local averaging and averaging over homogeneous directions.

the x direction. From $k_0x = 0.9$ to $k_0x = 3.3$, amplification of E_{11} is observed to be at higher and smaller wavenumbers. Figure 18(*c*) shows that E_{22} is more enhanced at small scales across the shock, which is similar to the observation of Lee *et al.* (1993). Further downstream, the spectrum drops over the entire range of wavenumbers.

Figure 18(*d*) shows the evolution of the one-dimensional energy spectra of the SGS kinetic energy. Interestingly, the evolution of E_{kk} shows more activity at small scales. For example, E_{kk} is magnified more at high wavenumbers from $k_0x = -1.5$ to $k_0x = 0.9$ and $k_0x = 3.3$, and decays faster at small scales from $k_0x = 3.3$ to $k_0x = 11.3$ and to $k_0x = 19.3$. At $k_0x = 3.3$, the spectrum is enhanced by more than one order of magnitude, and the small scales possess as high energy as the large scales.

5.3.4. *Localization*

The DSM (Germano *et al.* 1991; Moin *et al.* 1991) is known to require regularization to ensure stability. Averaging over homogeneous directions is most common. Such averaging is not practicable for flows without homogeneous directions or flow solvers that use unstructured girds. The proposed dynamic k-equation model appears to have an advantage over the DSM in that it is stable during the use of local averaging over the neighbouring CVs for the dynamic procedures. Figure 19 compares the results of the k-equation model derived from local averaging and averaging over homogeneous directions. When locally averaged, the model is slightly less dissipative, so that the decay rate of turbulent energy (intensities) is slightly slower at the inflow and downstream of the shock. Similar behaviour of the decay rate of turbulent kinetic energy is also observed in simulations of temporally and spatially decaying isotropic turbulence when local averaging is used, and is considered reasonable. Local averaging over-predicts the turbulent intensities a little bit more than homogeneous averaging far downstream, but the difference is still small. The robustness of the localized k-equation model may be attributed to two reasons. First, the performance (in terms of the resolved field) of the k-equation model is less sensitive to k even for initial value problems (figure 6). Second, the introduction of the k-equation introduces history effects into the SGS kinetic energy, so that the change of k is milder than in the Yoshizawa model, which is more sensitive to the instantaneous flow condition and grid resolution. As shown in figure 20, in the shock near field, where the mesh is clustered

https://doi.org/10.1017/jfm.2012.115 Published online by Cambridge University Press

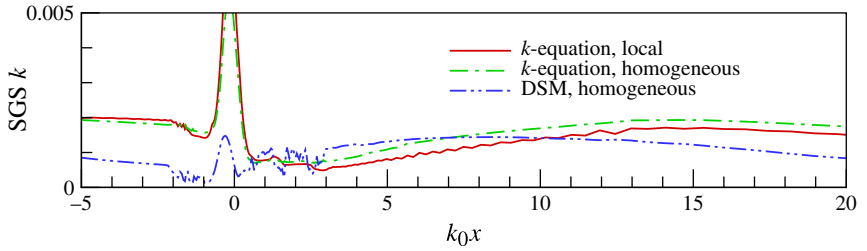


FIGURE 20. (Colour online) Distribution of mean SGS kinetic energy for the high-Re case of shock–turbulence interaction.

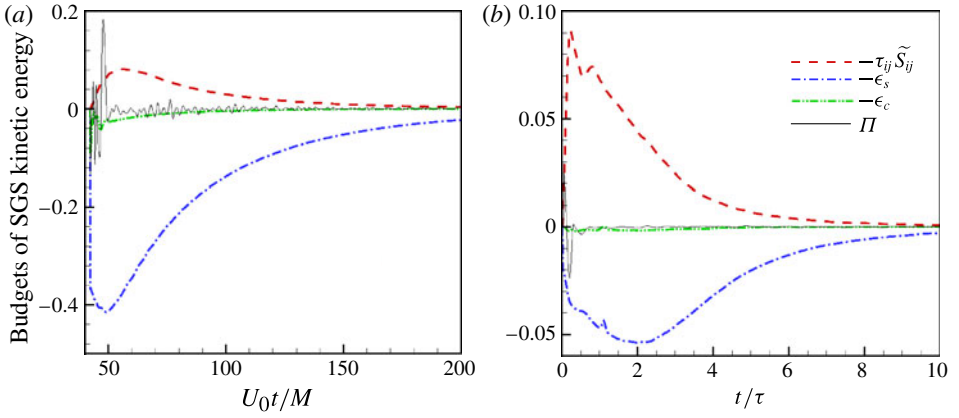


FIGURE 21. (Colour online) Budget of SGS k-equation for the decaying isotropic turbulence: (a) CBC; (b) compressible case with $M_t = 0.6$ initially.

and the interaction is also more intense, much more oscillation in the mean SGS kinetic energy is observed for the DSM than the k-equation model using either local or homogeneous averaging. The unphysical oscillation of the SGS kinetic energy in the DSM may well generate locally small or high eddy viscosity, and cause unexpected numerical instability. The overall performance of the localized dynamic k-equation model is promising, which facilitates its application to simulations of complex flow fields on unstructured grids.

6. Relevance of dilatational dissipation and pressure dilatation terms

The pressure dilatation term and dilatational dissipation term are the primary terms that differentiate the compressible SGS kinetic energy equation from its incompressible counterpart. To evaluate their relevance, the budgets of terms in the SGS kinetic energy equation are studied. Figure 21 shows the temporal evolution of each term on the right-hand side of the SGS kinetic energy equation for decaying isotropic turbulence. All the terms are normalized by $\rho u_{rms}^2/\tau$ at $t = 0$. Figure 21(a) is for CBC isotropic turbulence, and figure 21(b) is for the highly compressible case with initial $M_t = 0.6$ and $Re_\lambda = 67.6$. Owing to spatial homogeneity, the spatial average of terms in divergence form in the SGS kinetic energy equation is zero, and thus these terms are not plotted. As shown in figure 21(a), the terms ϵ_s and $-\tau_{ij}\widetilde{S}_{ij}$ are the most prominent terms. The term $-\tau_{ij}\widetilde{S}_{ij}$ is the SGS dissipation term in the

https://doi.org/10.1017/jfm.2012.115 Published online by Cambridge University Press

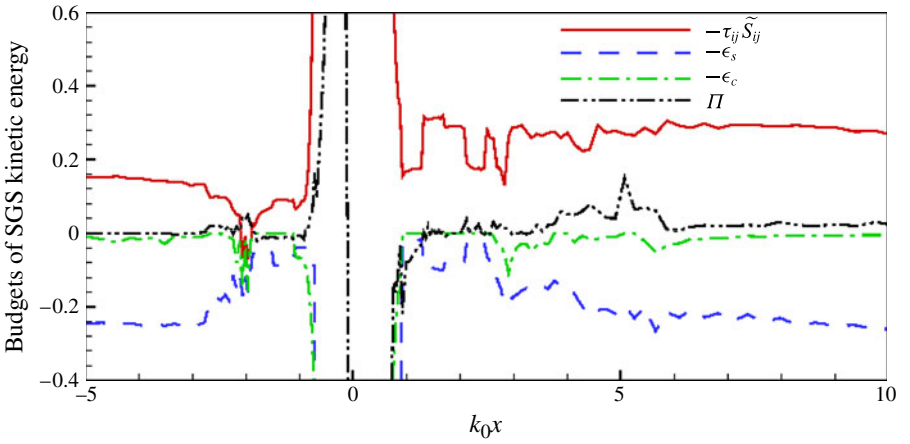


FIGURE 22. (Colour online) Budgets of SGS kinetic energy for shock–turbulence interaction.

transport equation for resolved kinetic energy (Piomelli *et al.* 1991), and acts as the production term for the SGS kinetic energy. The term ϵ_s is the dissipation term and is consistently larger than $-\tau_{ij}\widetilde{S}_{ij}$, which causes the SGS kinetic energy to decay. Both the magnitudes of ϵ_s and $-\tau_{ij}\widetilde{S}_{ij}$, as well as the difference between them, decrease temporally, which results in a reducing decay rate of SGS kinetic energy as observed in figure 5(*a*). Large initial transients are observed for pressure dilatation Π, which is due to the forced incompressible behaviour in the initial condition (inconsistent initial condition; Ristorcelli 1997). Similar transient behaviour can also be observed for ϵ_c, but the magnitude is much smaller. Figure 21(*b*) shows that, in the highly compressible simulation, these terms behave similarly to the quasi-incompressible case, except that the production term $-\tau_{ij}\widetilde{S}_{ij}$ is higher than the dissipation term ϵ_s initially. So the SGS kinetic energy will increase at the beginning, then decay afterwards, as shown in figure 8(*a*).

Figure 22 shows the budgets of the SGS kinetic energy equation for shock–turbulence interaction with high Re and high M_t. All the curves in figure 22 are normalized by $\rho k/\tau$ at the inlet, where k is the SGS kinetic energy, and τ is the eddy turnover time of the inflow turbulence. The whole domain can be approximately divided into three regions: before shock ($k_0x < -0.8$), intermittency region ($-0.8 < k_0x < 0.8$) and post-shock ($k_0x > 0.8$). Here, we focus on the regions before and after the shock wave. Before the shock, the flow is essentially spatially decaying isotropic turbulence, and the relevance of these four terms is similar to temporally decaying isotropic turbulence. In the near field ahead of the shock, all the terms drop in magnitude due to the clustered mesh. In the vicinity of the shock, all of the terms increase significantly due to intermittency. Downstream of the shock, the magnitude of the production term $-\tau_{ij}\widetilde{S}_{ij}$ is higher than that before the shock; while the solenoidal dissipation ϵ_s keeps similar levels as before. It appears that both pressure dilatation Π and dilatational dissipation ϵ_c become more important across the shock. Far downstream, ϵ_c and Π decrease in magnitude, and the four terms behave similarly to decaying turbulence.

From the analysis of the budgets of the SGS kinetic energy equation, we see that the dilatational dissipation term has negligible effect on the SGS turbulence away from the shock. However, across a shock the dilatational dissipation becomes important.

https://doi.org/10.1017/jfm.2012.115 Published online by Cambridge University Press

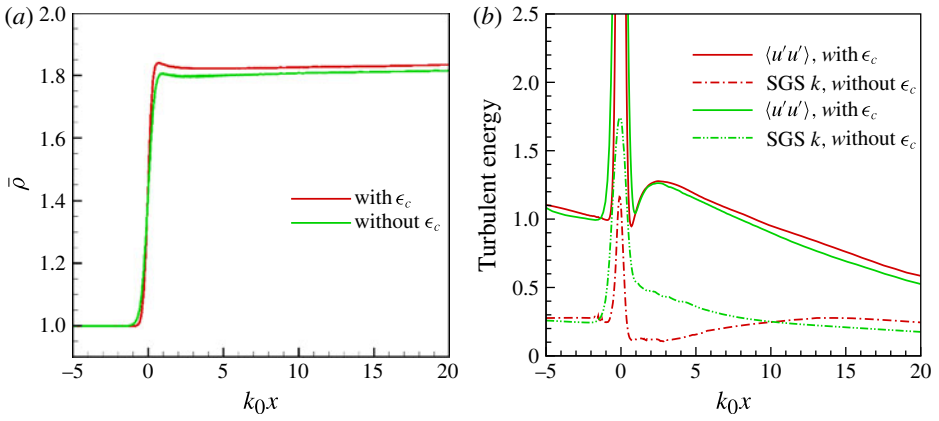


FIGURE 23. (Colour online) Effect of dilatational dissipation ϵ_c, on (*a*) the mean density and (*b*) the turbulent intensity.

Also the pressure dilatation term is important during the acoustic transient, but may have limited effect in the mean. To confirm our observation, we perform simulations with/without pressure dilatation and dilatational dissipation separately.

For the decaying isotropic turbulence, it is found that turning these two terms on and off does not make a discernible difference to both the resolved and the SGS field (not shown here), which is consistent with our observation that ϵ_c is negligible relative to ϵ_s, and the net effect of Π, which oscillates around zero, is small. For shock–turbulence interaction, without the pressure dilatation model, the results almost collapse onto those shown in figure 17. However, without dilatational dissipation, both the mean and fluctuation field will be affected. Figure 23 compares the mean density and turbulent energy distributions along the streamwise direction for shock–turbulence interaction between dynamic k-equation models with and without the dilatational dissipation term. In figure 23(*b*), it appears that, without dilatational dissipation, the dissipation of the SGS kinetic energy across the shock will not be enough. So, the the SGS kinetic energy after the shock relaxes too slowly to its normal value. High SGS kinetic energy will generate larger eddy viscosity and dissipate more of the turbulent intensities after the shock. Furthermore, through the total energy equation, this effect will be passed on to the mean flow field as shown in figure 23(*a*). Though the pressure dilatation term appears to have less effect on the mean profiles, this trend should not be assumed to hold for other problems. It does appear to be important instantaneously when acoustic interactions become significant.

7. Conclusions

A dynamic one-equation eddy viscosity model for compressible LES is proposed. The SGS kinetic energy transport equation is formally derived, and the residual terms in the filtered total energy equation that are neglected in the standard DSM have been revisited. The unclosed terms are modelled and the model coefficients are determined dynamically. An algebraic model based on series expansion is proposed for the pressure dilatation term, and a different dynamic procedure for the dissipation terms in energy equations is suggested. *A priori* tests using DNS of decaying isotropic turbulence are performed, which shows that the proposed dynamic k-equation model has comparable correlation level in the SGS stress and SGS heat flux to the DSM

https://doi.org/10.1017/jfm.2012.115 Published online by Cambridge University Press

model, and the suggested model for pressure dilatation correlates well with its actual value. The proposed dynamic k-equation model is applied to the decaying isotropic turbulence and isotropic turbulence–normal shock interaction problems in *a posteriori* tests. When compared to available experimental and DNS results, the k-equation model shows good agreement. It improves energy spectra at high wavenumbers for decaying isotropic turbulence, and it performs similarly to the DSM in shock–turbulence interaction because of the dominant linear effect. In shock–turbulence interaction, the one-dimensional energy spectra of resolved velocity components and the SGS kinetic energy are examined, and the behaviour of the SGS kinetic energy across the shock is discussed. The budget of the SGS kinetic energy equation shows that the dilatational dissipation is important for shock–turbulence interaction, but may be less important for decaying isotropic turbulence. The pressure dilatation term does not seem to have noticeable net effects in the mean, but instantaneously its magnitude is comparable to other dominant terms, especially when acoustic transients are present. In addition, the proposed dynamic k-equation model requires less regularization for stability, and is able to be localized easily without degrading its performance, which is encouraging for simulations of high-speed flows in complex geometries.

Acknowledgements

This work is supported by the National Science Foundation under grant CTS-0933377. Computer time for the simulations was provided by the Minnesota Supercomputing Institute (MSI), the National Institute for Computational Sciences (NICS) and the Texas Advanced Computing Center (TACC). We would like to thank Dr N. Park for his help during the early stages of this work.

REFERENCES

BEDFORD, K. W. & YEO, W. K. 1993 Conjunctive filtering procedures in surface water flow and transport. In *Large Eddy Simulation of Complex Engineering and Geophysical Flows* (ed. B. Galperin & S. A. Orszag), pp. 513–539. Cambridge University Press.

CHAI, X. & MAHESH, K. 2011 Simulations of high speed jets in cross-flows. *AIAA Paper* 2011-650.

CHOLLET, J. P. & LESIEUR, M. 1981 Parametrization of small scales of three-dimensional isotropic turbulence utilizing spectral closures. *J. Atmos. Sci.* **38**, 2747–2757.

COMTE-BELLOT, G. & CORRSIN, S. 1971 Simple Eulerian time correlation of full- and narrow-band velocity signals in grid-generated isotropic turbulence. *J. Fluid Mech.* **48**, 273.

DEARDORFF, J. W. 1973 Three-dimensional numerical modeling of the planetary boundary layer. In *Workshop on Micrometeorology* (ed. D. A. Haugen), pp. 271–311. American Meteorological Society.

DUBOIS, T., DOMARADZKI, J. A. & HONEIN, A. 2002 The subgrid-scale estimation model applied to large eddy simulations of compressible turbulence. *Phys. Fluids* **14** (5), 1781–1801.

ERLEBACHER, G., HUSSAINI, M. Y., KREISS, H. O. & SARKAR, S. 1990 The analysis and simulation of compressible turbulence. *Theor. Comput. Fluid Dyn.* **2**, 73–95.

GARNIER, E., ADAMS, N. & SAGAUT, P. 2009 *Large Eddy Simulation for Compressible Flows (Scientific Computation)*, 1st edn. Springer.

GÉNIN, F. & MENON, S. 2010 Dynamics of sonic jet injection into supersonic cross-flow. *J. Turbul.* **11**, 1–13.

GERMANO, M., PIOMELLI, U., MOIN, P. & CABOT, M. 1991 A dynamic subgrid-scale eddy viscosity model. *Phys. Fluids* **3**, 1760.

GHOSAL, S., LUND, T. S., MOIN, P. & AKSELVOLL, K. 1995 A dynamic localization model for large-eddy simulation of turbulent flows. *J. Fluid Mech.* **286**, 229.

https://doi.org/10.1017/jfm.2012.115 Published online by Cambridge University Press

GHOSH, S. & MAHESH, K. 2008 Numerical simulation of the fluid dynamic effects of laser energy deposition in air. *J. Fluid Mech.* **605**, 329–354.

HORIUTI, K. 1985 Large eddy simulation of turbulent channel flow by one-equation modeling. *J. Phys. Soc. Japan* **54**, 2855–2865.

KRAICHNAN, R. H. 1964 Direct-interaction approximation for shear and thermally driven turbulence. *Phys. Fluids* **7** (7), 1048–1062.

KRAICHNAN, R. H. 1976 Eddy viscosity in two and three dimensions. *J. Atmos. Sci.* **33**, 1521–1536.

LARSSON, J. & LELE, S. K. 2009 Direct numerical simulation of canonical shock/turbulence interaction. *Phys. Fluids* **21**, 126101.

LEE, S., LELE, S. K. & MOIN, P. 1993 Direct numerical simulation of isotropic turbulence interacting with a weak shock wave. *J. Fluid Mech.* **251**, 533–562.

LESIEUR, M. & MÉTAIS, O. 1996 New trends in large-eddy simulations of turbulence. *Annu. Rev. Fluid Mech.* **28**, 45–82.

LILLY, D. K. 1967 The representation of small-scale turbulence in numerical simulation experiments. In *IBM Scientific Computing Symposium on Environmental Sciences, Yorktown Heights*, pp. 195–210. IBM.

LILLY, D. K. 1991 A proposed modification of the Germano subgrid-scale closure method. *Phys. Fluids* A **3**, 1760.

MAHESH, K., LELE, S. K. & MOIN, P. 1997 The influence of entropy fluctuations on the interaction of turbulence with a shock wave. *J. Fluid Mech.* **334**, 353–379.

MASON, P. J. 1994 Large-eddy simulation: a critical review of the technique. *Q. J. R. Meteorol. Soc.* **120** (515), 1–26.

MENEVEAU, C. 1994 Statistics of turbulence subgrid-scale stresses: necessary conditions and experimental tests. *Phys. Fluids* **6** (2), 815–833.

MENEVEAU, C. & KATZ, J. 2000 Scale-invariance and turbulence models for large-eddy simulation. *Annu. Rev. Fluid Mech.* **32** (1), 1–32.

MENON, S. & KIM, W. W. 1996 High Reynolds number flow simulations using the localized dynamic subgrid-scale model. In *AIAA 34th Aerospace Sciences Meeting and Exhibit. AIAA Paper* 1996-0425.

MÉTAIS, O. & LESIEUR, M. 1992 Spectral large-eddy simulation of isotropic and stably stratified turbulence. *J. Fluid Mech.* **239**, 157–194.

MOENG, C.-H. 1984 A large-eddy-simulation model for the study of planetary boundary-layer turbulence. *J. Atmos. Sci.* **41**, 2052–2062.

MOIN, P., SQUIRES, K., CABOT, W. & LEE, S. 1991 A dynamic subgrid-scale model for compressible turbulence and scalar transport. *Phys. Fluids* A **3** (11), 2746–2757.

MUPPIDI, S. & MAHESH, K. 2011 DNS of roughness-induced transition in supersonic boundary layers. *J. Fluid Mech.* **693**, 28–56.

PARK, N. & MAHESH, K. 2007 Numerical and modeling issues in LES of compressible turbulent flows on unstructured grids. *AIAA Paper* 2007-0722.

PIOMELLI, U., CABOT, W. H., MOIN, P. & LEE, S. 1991 Subgrid-scale backscatter in turbulent and transitional flows. *Phys. Fluids* A **3**, 1766–1771.

POMRANING, E. & RUTLAND, C. J. 2002 Dynamic one-equation nonviscosity large-eddy simulation model. *AIAA J.* **40**, 689–701.

RISTORCELLI, J. R. 1997 A pseudo-sound constitutive relationship for the dilatational covariances in compressible turbulence. *J. Fluid Mech.* **347**, 37–70.

RISTORCELLI, J. R. & BLAISDELL, G. A. 1997 Consistent initial conditions for the DNS of compressible turbulence. *Phys. Fluids* **9** (1), 4–6.

SARKAR, S., ERLEBACHER, G., HUSSAINI, M. Y. & KREISS, H. O. 1991 The analysis and modeling of dilatational terms in compressible turbulence. *J. Fluid Mech.* **227**, 473–493.

SCHUMANN, U. 1975 Subgrid scale model for finite difference simulations of turbulent flows in plane channels and annuli. *J. Comput. Phys.* **18** (4), 376–404.

SHAW, R. H. & SCHUMANN, U. 1992 Large-eddy simulation of turbulent flow above and within a forest. *Boundary-Layer Meteorol.* **61**, 47–64.

https://doi.org/10.1017/jfm.2012.115 Published online by Cambridge University Press

SMAGORINSKY, J. 1963 General circulation experiments with the primitive equations. I. The basic experiment. *Mon. Weath. Rev.* **91**, 99–165.

SMITH, L. M. & WOODRUFF, S. L. 1998 Renormaliztion-group analysis of turbulence. *Annu. Rev. Fluid Mech.* **30**, 275–310.

SPEZIALE, C. G. 1991 Analytic methods for the development of Reynolds-stress closures in turbulence. *Annu. Rev. Fluid Mech.* **23**, 107–157.

SPEZIALE, C. G., ERLEBACHER, G., ZANG, T. A. & HUSSAINI, M. Y. 1988 The subgrid-scale modeling of compressible turbulence. *Phys. Fluids* **31** (4), 940–942.

SPYROPOULOS, E. T. & BLAISDELL, G. A. 1996 Evaluation of the dynamic model for simulations of compressible decaying isotropic turbulence. *AIAA J.* **34** (5), 990–998.

VREMAN, B., GEURTS, B. & KUERTEN, H. 1995 Subgrid-modeling in LES of compressible flow. *Appl. Sci. Res.* **54**, 191–203.

YAKHOT, A., ORSZAG, S. A. & YAKHOT, Y. 1989 Renormalization-group formulation of large-eddy simulations. *J. Sci. Comput.* **4**, 139.

YEE, H. C, SANDHAM, N. D & DJOMEHRI, M. J 1999 Low-dissipative high-order shock-capturing methods using characteristic-based filters. *J. Comput. Phys.* **150** (1), 199–238.

YOSHIZAWA, A. 1986 Statistical theory for compressible turbulent shear flows, with the application to subgrid modeling. *Phys. Fluids* **29**, 2152.

YOSHIZAWA, A. & HORIUTI, K. 1985 A statistically-derived subgrid-scale kinetic energy model for the large-eddy simulation of turbulent flows. *J. Phys. Soc. Japan* **54**, 2834–2839.

https://doi.org/10.1017/jfm.2012.115 Published online by Cambridge University Press